PHYSICAL REVIEW C **83**, 015505 (2011)

Measurement of parity-violating γ-ray asymmetry in the capture of polarized cold neutrons on protons

M. T. Gericke,[1] R. Alarcon,[2] S. Balascuta,[2] L. Barrón-Palos,[3] C. Blessinger,[4] J. D. Bowman,[4,*] R. D. Carlini,[5] W. Chen,[6]
T. E. Chupp,[7] C. Crawford,[8] S. Covrig,[5] M. Dabaghyan,[9] N. Fomin,[10] S. J. Freedman,[11] T. R. Gentile,[6] R. C. Gillis,[12,13]
G. L. Greene,[4,10] F. W. Hersman,[9] T. Ino,[14] G. L. Jones,[15] B. Lauss,[16] M. Leuschner,[17] W. R. Lozowski,[12,13] R. Mahurin,[1,5]
Y. Masuda,[14] J. Mei,[5] G. S. Mitchell,[18] S. Muto,[14] H. Nann,[12,13] S. A. Page,[1] S. I. Penttilä,[4] W. D. Ramsay,[1,19] A. Salas-Bacci,[20]
S. Santra,[21] M. Sharma,[7] P.-N. Seo,[22] E. I. Sharapov,[23] T. B. Smith,[24] W. M. Snow,[12,13,†] W. S. Wilburn,[20] and V. Yuan[20]
(NPDGamma Collaboration)
[1]*University of Manitoba, Winnipeg, MB, Canada R3T 2N2*
[2]*Arizona State University, Tempe, AZ 85287, USA*
[3]*Universidad Nacional Autónoma de México, C.P. 04510, Mexico, D.F.*
[4]*Oak Ridge National Laboratory, Oak Ridge, TN 37831, USA*
[5]*Thomas Jefferson National Accelerator Facility, Newport News, VA 23606, USA*
[6]*National Institute of Standards and Technology, Gaithersburg, MD 20899-0001,USA*
[7]*University of Michigan, Ann Arbor, MI 48104, USA*
[8]*University of Kentucky, Lexington, Kentucky 40506, USA*
[9]*University of New Hampshire, Durham, NH 03824, USA*
[10]*University of Tennessee, Knoxville, TN 37996, USA*
[11]*University of California, Berkeley, CA 94720-7300, USA*
[12]*Indiana University, Bloomington, IN 47405, USA*
[13]*Center for the Exploration of Energy and Matter, Bloomington, IN 47408, USA*
[14]*High Energy Accelerator Research Organization (KEK), Tukuba-shi, 305-0801, Japan*
[15]*Hamilton College, Clinton, NY 13323, USA*
[16]*Paul Scherrer Institut, CH-5232 Villigen, Switzerland*
[17]*Procure Treatment Center, 420 N. Walnut St., Bloomington, IN 47404-3803, USA*
[18]*Department of Biomedical Engineering, University of California, Davis, CA 95616, USA*
[19]*TRIUMF, 4004 Wesbrook Mall, Vancouver, BC, Canada V6T 2A3*
[20]*Los Alamos National Laboratory, Los Alamos, NM 87545, USA*
[21]*Bhabha Atomic Research Center, Trombay, Mumbai 400085, India*
[22]*Department of Physics, North Carolina State University, Raleigh, NC 27695, USA*
[23]*Joint Institute for Nuclear Research, Dubna, Russia*
[24]*University of Dayton, Dayton, OH 45469, USA*

(Received 1 March 2010; revised manuscript received 1 November 2010; published 31 January 2011)

The NPDGamma collaboration reports results from the first phase of a measurement of the parity violating up-down asymmetry A_γ with respect to the neutron spin direction of γ rays emitted in the reaction $\vec{n} + p \rightarrow d + \gamma$ using the capture of polarized cold neutrons on the protons in a liquid parahydrogen target. One expects parity-odd effects in the hadronic weak interaction between nucleons to be induced by the weak interaction between quarks. A_γ in $\vec{n} + p \rightarrow d + \gamma$ is dominated by a $\Delta I = 1$, ${}^3S_1$-${}^3P_1$ parity-odd transition amplitude in the *n*-*p* system. The first phase of the measurement was completed at the Los Alamos Neutron Science Center spallation source (LANSCE), with the result $A_\gamma = [-1.2 \pm 2.1\ (\text{stat.}) \pm 0.2\ (\text{sys.})] \times 10^{-7}$. We also report the first measurement of an upper limit for the parity-allowed left-right asymmetry in this reaction, with the result $A_{\gamma,\text{LR}} = [-1.8 \pm 1.9\ (\text{stat.}) \pm 0.2\ (\text{sys.})] \times 10^{-7}$. In this paper we give a detailed report on the theoretical background, experimental setup, measurements, extraction of parity-odd and parity-allowed asymmetries, analysis of potential systematic effects, and LANSCE results. The asymmetry has an estimated size of 5×10^{-8} and the aim of the NPDGamma collaboration is to measure it to 1×10^{-8}. The second phase of the measurement will be performed at the Spallation Neutron Source at Oak Ridge National Laboratory.

DOI: 10.1103/PhysRevC.83.015505 PACS number(s): 13.75.Cs, 11.30.Er, 24.70.+s, 24.80.+y

I. INTRODUCTION

We report on the first phase of a new measurement of the parity-violating (PV) γ-ray asymmetry in the radiative capture of polarized cold neutrons on protons in a liquid parahydrogen target. This asymmetry is dominated by a $\Delta I = 1$ parity-odd transition amplitude in the ${}^3S_1$-${}^3P_1$ channel expected from the strangeness-conserving hadronic weak interaction (HWI) between nucleons. Because this transition is accessible through pion exchange, which dominates the low-energy strong interactions between nucleons owing to chiral

---

[*] Spokesperson

[†] Corresponding author: wsnow@indiana.edu

symmetry breaking in quantum chromodynamics (QCD), it is clear that this amplitude is an essential part of any description of the HWI for energies small compared to the strong QCD scale $\Lambda = 1$ GeV.

The HWI in general and the *NN* weak interaction amplitudes in particular are scientifically interesting for several reasons [1–5]. Because the range for W and Z exchange between quarks is small compared to the nucleon size, HWIs are first order sensitive to quark-quark correlations in hadrons. This is also true for strangeness-changing nonleptonic weak decays of hadrons. Both nonleptonic weak kaon decays (which have been known for decades to be greatly amplified in the $\Delta I = 1/2$ channel) and nonleptonic weak decays of hyperons exhibit deviations from the expected relative sizes of weak amplitudes whose dynamical source is still not fully understood [6]. If these unexpected patterns in the isospin dependence of nonleptonic weak amplitudes are confirmed by measurements in the *NN* and few nucleon systems, it would indicate that this dynamical puzzle operates for all light quarks (rather than just the strange quark) and is therefore a nontrivial QCD dynamical phenomenon of general interest [1]. The weak *NN* interaction is also one of the few systems thought to be sensitive to quark-quark neutral current effects at low energy, as charged currents are suppressed in $\Delta I = 1$ *NN* processes by $V_{\mathrm{us}}^2/V_{\mathrm{ud}}^2 \simeq 0.1$. Quark-quark and *NN* weak interactions also induce parity-odd effects in electron scattering [7–10], nuclear decays [11], compound nuclear resonances [12,13], and atomic structure, where they are the microscopic source for nuclear anapole moments [14–17]. The comparison between *NN* weak amplitudes in few nucleon systems and heavy nuclei can also offer theoretical insight into the relative importance of possible heavy Majorana particle exchange in neutrinoless double β decay [18].

QCD possesses only vector interactions and its gauge symmetry is unbroken in its low-temperature phase, and in this phase QCD is therefore expected to conserve parity (it is suspected that QCD can spontaneously break parity symmetry in high-temperature phases [19]). The residual PV HWI is therefore expected to be induced only by quark-quark weak interactions as described in the standard model. There are two model-independent statements that one can make about this interaction: one at the quark level, for energies above Λ, and the other at the nucleon level, for energies below Λ. For energies above Λ but below the electroweak scale, the quark-quark weak interaction can be written in a current-current form with pieces that transform under (strong) isospin as $\Delta I = 0, 1, 2$. At the nucleon level for energies below Λ, one can show that five independent weak transition amplitudes are present in *NN* elastic scattering at low energy [20]: the $\Delta I = 1$ transition amplitudes between ${}^3S_1$-${}^3P_1$ and ${}^1S_0$-${}^3P_0$ partial waves; the $\Delta I = 0$ transition amplitudes between ${}^3S_1$-${}^1P_1$ and ${}^1S_0$-${}^3P_0$ partial waves; and the $\Delta I = 2$ transition amplitude between ${}^1S_0$-${}^3P_0$ partial waves. Unfortunately it is not yet possible to perform a quantitative calculation in the standard model to interpolate between these two limits.

The relative strengths of the different four-quark operators just below the electroweak scale evolve under the QCD renormalization group and can be calculated in QCD perturbation theory [21,22] between the electroweak scale and Λ. However, the unsolved nonperturbative QCD dynamics has so far prevented theorists from extending these calculations below Λ to make direct contact with low-energy *NN* weak amplitudes. If one wants to probe the nonperturbative physics of the ground state of an asymptotically free gauge theory like QCD, an interaction that is weak, perturbative, and calculable at a short distance, and does not itself significantly affect the strong dynamics, is exactly the type of probe one wants to employ. The development of quark-quark weak interactions into *NN* weak interactions as the distance scale increases satisfies these criteria. It is in this sense that measurements of the *NN* weak interaction can be thought of as an “inside-out” probe of the ground state of QCD.

Theoretical work on the HWI can be organized into three broad classes, depending on how the strong interaction dynamics are treated: (1) model-dependent approaches that posit a specific dynamical mechanism for the interaction, (2) model-independent approaches with a direct connection to QCD based on its symmetries, and (3) direct calculation from the standard model. Model-dependent approaches include meson exchange, QCD sum rules [23–25], nonlocal chiral quark models [26], SU(3) Skyrme models [27], and models motivated by the recent nonperturbative treatment of QCD based on the AdS/CFT correspondence [28]. In the meson exchange picture the *NN* weak interaction is modeled as a process in which the three lightest mesons (π, ρ, and ω) couple to one nucleon via the weak interaction at one vertex and to the second nucleon via the strong interaction at the other vertex. An attempt to calculate the weak meson-nucleon couplings of the HWI from the standard model using a valence quark model for QCD that was first made by Desplanques, Donoghue, and Holstein (the DDH paper [29]) in 1980 and later updated [30]. In the DDH model HWI observables are expressed in terms of six weak meson-nucleon coupling constants—h_π^1, h_ρ^0, h_ρ^1, h_ρ^2, h_ω^0, and h_ω^1—where the subscript indicates the exchange meson and the superscript labels the isospin change. The results obtained by DDH have served as a de facto benchmark for experimental and theoretical work in the field for several years. An experimental program was outlined and the calculations specifying the relation between the corresponding observables and the weak coupling constants were reviewed, compiled, and, in some cases, performed by Adelberger and Haxton in 1985 [11].

More recently a model-independent theoretical framework has spurred renewed theoretical interest and experimental effort. This framework is based on effective field theory (EFT) methods that have been applied with success to low-energy processes in the meson and nucleon sectors and have now been extended to describe the HWI. It has the advantage of being, by construction, the most general theoretical description consistent with the symmetries and degrees of freedom of low-energy QCD, and it involves within this framework a perturbative expansion in the small parameter p/Λ, where p is a typical internal momentum involved in the reaction. Because NPDGamma and several other planned experiments to resolve *NN* weak interaction effects occur in this energy range, one can imagine determining the unknown couplings of the operators in the EFT description from experiment. The theory takes different forms depending on the treatment of strong interaction effects and whether or not pions are treated as separate dynamical degrees of freedom. For processes in which the momentum transfers involved are below ≈40 MeV a pionless EFT is appropriate, whereas for higher momenta it becomes important to include explicit pion degrees of freedom. One version [1,5,31], termed a "hybrid" EFT, treats the weak interaction with nucleon contact interactions parameterized in terms of 12 coupling constants that specify the strength of 12 possible parity-odd, time-reversal even four-nucleon terms in the Lagrangian and implements the strong interaction using *NN* potentials. The low-energy limit of the pionful version of this theory possesses six independent parameters: five weak *S*-*P* transition amplitudes ($\lambda_S^{0,1,2}$, λ_T, and ρ_T), which reduce to the five parameters in the pionless version, and a longer-range term $\tilde{C}_6^\pi$ from explicit pion exchange (proportional to h_π^1 in DDH). Another EFT approach [32] treats both the strong and the weak interactions consistently in an EFT framework and possesses five parameters in the low-energy limit labeled by the partial wave transition amplitudes.

The possibility of calculating the weak *NN*amplitudes on the lattice was analyzed long ago [33] and is now under active investigation. The most easily accessible amplitude for lattice calculations is the long-range component in the $\Delta I = 1$, ${}^3S_1$-${}^3P_1$ channel, which is precisely the amplitude that the γ asymmetry in $\vec{n} + p \to d + \gamma$ measures. An effort to calculate parity violation in this partial wave on the lattice is listed as a "grand challenge" problem in exoscale computing [34]. In combination with the parallel efforts to calculate on the lattice the $\Delta I = 1/2$ and $\Delta I = 3/2$ amplitudes in nonleptonic kaon decay [35], the success of these efforts would offer the exciting possibility of a direct comparison of nontrivial nonleptonic weak interaction amplitudes with the standard model.

A nonzero PV asymmetry in neutron-proton capture has never been seen. The only experimentally known fact about this asymmetry is that it is smaller than $\approx 2 \times 10^{-7}$. This upper limit was established in the only previous measurement of this observable [$A_\gamma = (0.6 \pm 2.1) \times 10^{-7}$] [36] and the results presented in this paper. These results are consistent with the theoretically estimated size of the asymmetry in the DDH model ($\approx 5 \times 10^{-8}$). Because the deuteron-bound state and low-energy scattering states are dominated by the long-range components of the strong *NN* interaction, which are well understood experimentally, the relation between the asymmetry and the weak coupling in either model mentioned is stable against small variations in *NN* strong interaction parameters, which primarily affect the short-range components [5,29,31,37,38].

NPDGamma measures a weak amplitude between two nucleons and the interpretation of the measured result is free of possible uncertainties inherent in the theoretical treatment of nuclear many-body systems. The deuteron is the most loosely bound stable nuclear system and the asymmetry in the NPDGamma experiment therefore obtains its largest contribution from the longest-range weak nucleon-nucleon interaction, which, in the context of the meson exchange picture, corresponds to the pion-nucleon coupling [11,29]. With its expected final measurement accuracy of (1×10^{-8}), coupled with the existing theoretical estimates for the size of this weak coupling, the NPDGamma collaboration aims to make the first nonzero measurement of the asymmetry at the 20% level. We report here on the experimental setup, analysis, and results of the first phase measurement, which was completed in 2006 at the Los Alamos Neutron Science Center (LANSCE).

The remainder of the paper is organized as follows. We first provide a brief description of the amplitudes that contribute to the NPDGamma observable and how they relate to both the EFT and the weak meson exchange pictures. We then give a detailed overview of the experimental layout, describe the 2006 measurements and their analysis, outline our estimates of several possible sources of systematic error, and conclude with a discussion of the results.

II. NPDGAMMA THEORY

The goal of the NPDGamma experiment is to measure the long-range $\Delta I = 1$ part of the HWI in a two-body system where nuclear structure uncertainties are absent. In $\vec{n} + p \to d + \gamma$ the low energy of the initial two-nucleon state and the weak binding of the deuteron reduce the relative importance of short-range contributions, and the quantum numbers of the states involved isolate the $\Delta I = 1$ component of the HWI. The differential cross section in this simple system can be calculated explicitly from the transition amplitudes of the electromagnetic part of the Hamiltonian between initial (capture) and final (bound) two-nucleon states, which possess mixed parity owing to the *NN* weak interaction. In the $\vec{n} + p \to d + \gamma$ reaction, the most probable intermediate states produce γ rays through the parity-conserving *M*1 transition between the initial singlet and triplet *S*-wave states ${}^1S_0$, ${}^3S_1$ and the deuteron *n*-*p* bound state accessed through the strong *NN* interaction. The weak *NN* interaction mixes ${}^3P_1$, ${}^3P_0$, and ${}^1P_1$ *p*-wave components into the initial and final states that allow *E*1 γ transitions, and the interference between these *E*1 and *M*1 transitions gives rise to a parity-odd asymmetry in the γ angular distribution. The expression for the differential cross section (not including experimental factors discussed in detail in Sec. IV) is given by

$$\frac{d\sigma}{d\Omega} \propto \frac{1}{4\pi}(1 + A_\gamma \cos\theta), \tag{1}$$

where θ is the angle between the neutron spin direction and the γ-ray momentum.

In the absence of parity violation, $A_\gamma = 0$. A nonzero asymmetry A_γ in the angular distribution of 2.2-MeV γ rays with respect to the neutron spin direction can come from small non-parity-conserving admixtures of *P*-wave states in the primarily *S*-wave initial singlet and the final triplet states of the form

$$\epsilon = \frac{\langle \psi_{\alpha'} | W | \psi_\alpha \rangle}{\Delta E}, \tag{2}$$

where $\alpha = \{J, L, S, p\}$ ($p =$ parity) ranges over the allowed quantum numbers for the transitions. For the $\vec{n} + p \to d + \gamma$ reaction, it can be shown that there is a simple expression for the γ-ray γ ray asymmetry in terms of the matrix elements between initial and final states:

$$A_\gamma \propto \mathrm{Re}\frac{\epsilon\langle {}^3P_1|\mathbf{E1}|{}^3S_1\rangle}{\langle {}^3S_1|\mathbf{M1}|{}^1S_0\rangle}. \tag{3}$$

The parity-odd amplitudes $\langle\psi_{\alpha'}|W|\psi_\alpha\rangle$ can be treated to an excellent approximation as perturbations in this and all low-energy *NN* weak interaction processes. They can be estimated within the meson exchange picture (i.e., DDH) or other QCD models, parametrized using EFT, or calculated from the standard model using lattice gauge theory. In the meson exchange picture, an HWI observable (O_{PV}) can be expressed completely in terms of six weak meson-nucleon coupling constants: $O_{\mathrm{PV}} = a_\pi^1 h_\pi^1 + a_\rho^0 h_\rho^0 + a_\rho^1 h_\rho^1 + a_\rho^2 h_\rho^2 + a_\omega^0 h_\omega^0 + a_\omega^1 h_\omega^1$. The coefficients $a^{\Delta I}$ where ΔI is the change in isospin, are determined from theoretical calculations (for NPDGamma this would be the evaluation of electromagnetic matrix elements for the $\vec{n}+p\rightarrow d+\gamma$ reaction). In this model the only significant contribution to the NPDGamma asymmetry comes from weak pion exchange. The relation between the measured asymmetry and the DDH weak meson couplings is [5,11,38–41]

$$A_\gamma = -0.1069 h_\pi^1 - 0.0014 h_\rho^1 + 0.0044 h_\omega^1. \tag{4}$$

The interaction is therefore almost purely $\Delta I = 1$, as one would expect based on the allowed *n*-*p* continuum and bound states. These calculations also confirm that the effect of the *d*-state admixture in the deuteron ground state on these coefficients is negligible.

The $\Delta I = 1$ piece of the interaction accessed in $\vec{n}+p\rightarrow d+\gamma$ has been the subject of previous work. The predicted best value for h_π^1 is 4.7×10^{-7} [29]. The most sensitive experiments designed to search for the $\Delta I = 1$ weak *NN* channel using the ^{18}F γ-ray circular polarization [42] did not see any effect. Coupled with theoretical arguments [43] made in the context of the DDH model, one infers $h_\pi^1 \leqslant 1.2\times10^{-7}$. The nonzero measurement of the anapole moment of ^{133}Cs [14] has been used to extract $h_\pi^1 = [9.6\pm2.2\,(\mathrm{exp.})\pm 3.6\,(\mathrm{theor.})]\times10^{-7}$ [44]. The $\Delta I = 1$ part of the HWI therefore remains undetermined.

In EFT the $\vec{n}+p\rightarrow d+\gamma$ reaction is described by a contact interaction. At the very low energies involved in the NPDGamma process, this treatment is parametrized by a set of five low-energy coupling constants that, in the $E\rightarrow 0$ limit, are equivalent to the five Danilov parameters ($\lambda_S^{0,1,2}$, λ_T, and ρ_T) [45]. The NPDGamma asymmetry isolates the $\rho_t({}^3S_1\rightarrow{}^3P_1)$ long-range transition [5,31] in this language. Liu [5] gives

$$A_\gamma = -0.093 m_N \rho_t - 0.27\tilde{C}_6^\pi. \tag{5}$$

The pionless EFT expression is [46]

$$A_\gamma = \frac{32}{3}\frac{M}{(1-\gamma a^{{}^1S_0})}\frac{C^{{}^3S_1-{}^3P_1}}{C_0^{{}^3S_1}}, \tag{6}$$

where M is the nucleon mass, $\gamma = \sqrt{MB}$, with B the deuteron binding energy, and $a^{{}^1S_0}$ is the strong *NN* scattering length in the $^1S_0$ channel. The asymmetry depends on the ratio of the weak and strong low-energy constants (LECs) in the EFT Lagrangian: $C^{{}^3S_1\text{-}{}^3P_1}$ is the LEC associated with the corresponding operator induced by the weak interaction in the EFT Lagrangian, and $C_0^{{}^3S_1}$ is the LEC associated with the corresponding operator induced by the strong interaction in the EFT Lagrangian.

The advantage of the EFT formulation is that the LECs are calculable, in principle, using nonperturbative QCD and can be consistently employed in calculations of other processes involving HWIs in a well-defined manner. In addition, that portion of the strong QCD dynamics that is determined by chiral symmetry breaking is automatically included. It therefore will be easier to make a clear connection between the EFT parameters and the standard model, when nonperturbative calculations involving four-quark weak operators can eventually be performed using lattice QCD. However, as the EFT description makes no assumptions about the strong dynamics beyond the incorporation of QCD symmetries, the couplings in EFT are treated as completely free parameters. Within the spirit of this framework it is not immediately obvious that the short-range $\Delta I = 1$ couplings are small. Estimates of the possible short-range contributions to $\Delta I = 1$ processes within the EFT approach have recently been performed [47] using heavy baryon chiral perturbation theory to estimate the possible size of NNLO corrections to the lowest-order EFT prediction. For the $\vec{n}+p\rightarrow d+\gamma$ reaction the authors find these corrections to be no larger than 20% in size. Therefore in both the DDH and the EFT treatments the parity-odd γ asymmetry in $\vec{n}+p\rightarrow d+\gamma$ is dominated by only the $^3S_1$-$^3P_1$ parity-odd transition amplitude.

III. EXPERIMENT

Until the end of 2006 the NPDGamma apparatus was located on flight path 12 at the Manuel Lujan Jr. Neutron Scattering Center at LANSCE. Figure 1 shows a schematic of the flight path and experimental setup. The LANSCE linear accelerator delivers 800-MeV protons to a storage ring (PSR), which compresses the beam to 250-ns-wide pulses at the base. The protons from the PSR are incident on a split tungsten target at 20 Hz and the resulting spallation neutrons are cooled by and backscattered from a cold superthermal H_2 moderator with a surface area of 12×12 cm^2 [48]. The cold neutrons were transported to the experimental apparatus with an $m = 3$ supermirror neutron guide and then transversely polarized by transmission through a polarized ^{3}He cell. Three ^{3}He parallel-plate ion chambers were used to monitor beam intensity and polarization. A radio-frequency spin rotator was used to reverse the neutron spin direction on a pulse by pulse basis. The polarized neutrons were then captured on a liquid parahydrogen target placed in the center of the γ-detector array. The 2.2-MeV γ rays from the neutron capture were detected by an array of 48 CsI(Tl) detectors operated in current mode [49,50]. The entire apparatus was located in a homogeneous $\simeq$1-mT field to maintain the polarized ^{3}He gas used to polarize the neutrons and fix the neutron spin direction downstream of the polarizer. This field possessed a gradient of less than 1 μT/cm to make spin-dependent Stern-Gerlach steering of the polarized neutron beam negligible.

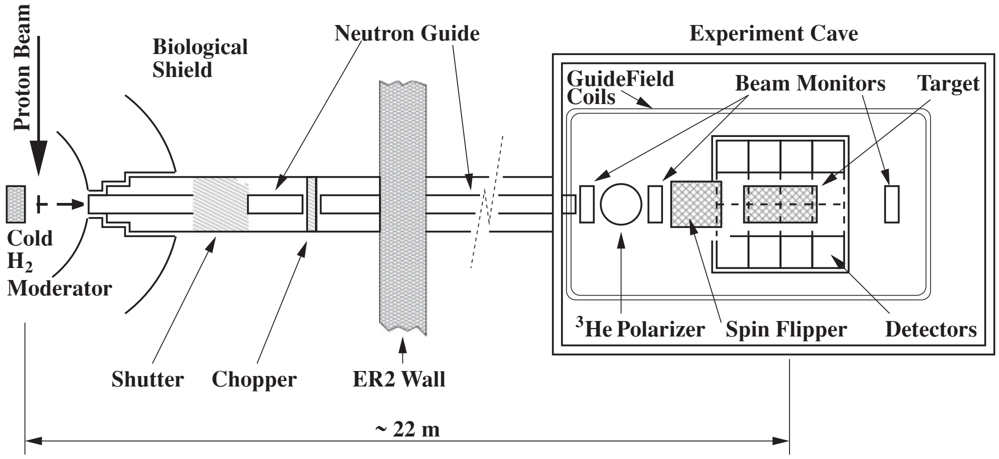

FIG. 1. Schematic of flight path 12 and the experimental setup of the NPDGamma experiment at LANSCE.

The distance between the moderator and the target is about 22 m. The flight path 12 (FP12) beam line consists of a neutron guide, a shutter, and a beam chopper. The pulsed spallation neutron source allowed us to measure the neutron time of flight and therefore determine the neutron energy. Within the 50-ms time-of-flight frame set by the source frequency, the chopper is used to define a time-of-flight region corresponding to a neutron energy range from 2 to 15 meV and to prevent neutrons from different frames from mixing and thus making the neutron energy information ambiguous. In this experiment the chopper was used to close the beam before the end of the frame, allowing us to take beam-off (pedestal) data for $\simeq$6 ms at the end of each neutron pulse. That portion of the data was used for detector pedestal and background studies (Fig. 2). After sampling of the detector array stops, the last 10 ms of the frame was used for data transfer from the data acquisition (DAQ) system. A detailed description of the FP12 neutron guide and its performance is given in Ref. [48]. The measured FP12 moderator brightness has a maximum of 1.25×10^8 n/(s $\cdot$ cm^2 $\cdot$ sr $\cdot$ meV $\cdot$ μA) for neutrons with an energy of 3.3 meV. The integrated capture flux of the neutrons at the end of the guide was measured to be 1.0×10^9 n/cm^2 s at an average proton current of 100 μA.

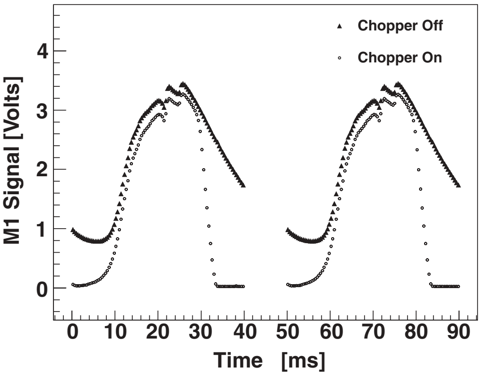

FIG. 2. Normalized signal from the first beam monitor downstream of the guide exit. Filled triangles show the signal obtained from a run where the chopper was parked open. Open circles correspond to a run taken with the chopper running.

Neutrons were polarized by passing through a 12-cm-diameter glass cell containing polarized ^{3}He [51,52], and references therein]. Beam polarization was measured with the beam monitors using relative neutron transmission and the ^{3}He polarization was monitored using NMR. For γ asymmetry measurements the figure of merit is the statistical accuracy that can be reached for a certain running time, which is proportional to the product $P_n\sqrt{T_n}$, where T_n is the neutron transmission through the ^{3}He cell and P_n is the neutron polarization [53]. Because the neutron absorption reaction cross section on ^{3}He is proportional to $1/\sqrt{E_n}$, where E_n is the neutron energy, the neutron transmission increases with energy, whereas the neutron polarization decreases with energy. In the data analysis the neutron polarization was calculated separately for each run by fitting the transmission spectrum to the expression $P_n = \tanh{(\sigma_c nl P_{\mathrm{He}})}$ [54], where $\sigma_c = \sigma_0\sqrt{(E_0/E_n)}$, with $\sigma_0 = 5333$ barns at the thermal energy $E_0 = 25.3$ meV and $nl = 4.84 \cdot 2.69 \times 10^{23}$ atoms/m^2 (see Fig. 3), where the ^{3}He thickness of 4.84 bar $\cdot$ cm was measured separately.

Most of the polarized neutrons then captured on the liquid parahydrogen target [55] were placed in the center of the γ detector array. The parahydrogen molecular state is required to ensure that the neutrons are not depolarized in the liquid hydrogen before capture. For neutron energies too low to excite the $J = L = S = 0$ parahydrogen molecules to the ground state of orthohydrogen, neutron spin-flip scattering is disallowed by conservation of angular momentum. The parahydrogen fraction in the liquid hydrogen target is monitored periodically using the energy spectrum of neutrons transmitted through the target along with the known energy dependence of the scattering cross sections from parahydrogen and orthohydrogen molecules [56]. With a 99.98% parahydrogen fraction, about 60% of the neutrons that enter the target are captured on hydrogen. The detector array consists of 48 CsI(Tl) cubes, with a 15-cm side length, arranged in a cylindrical pattern in four rings of 12 detectors each around the target area (Fig. 4). In addition to the conditions set on the detector array by the need to preserve statistical accuracy and suppress systematic

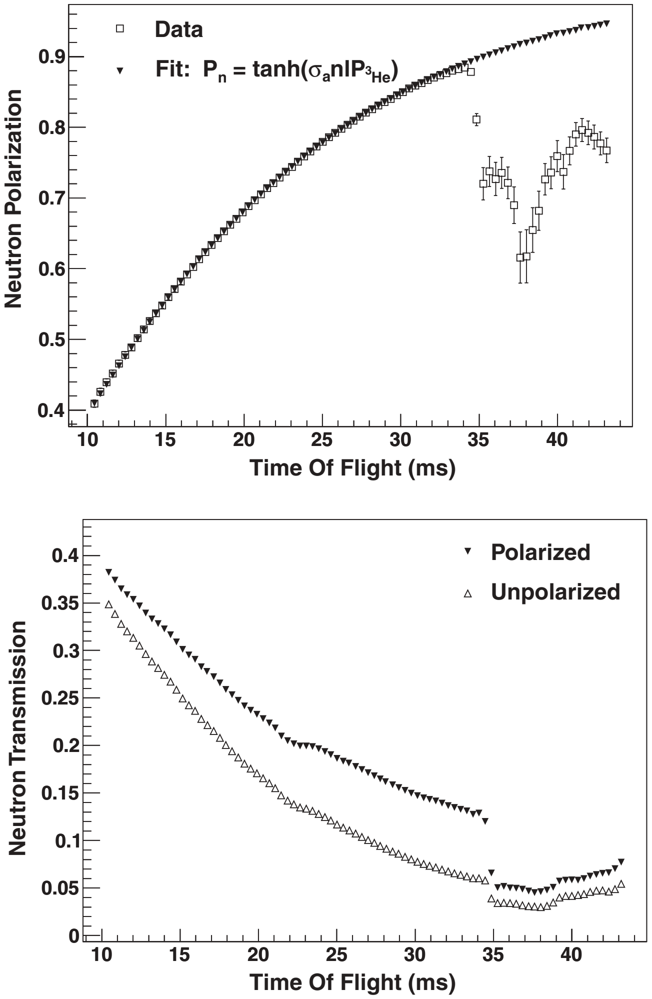

FIG. 3. Top: Plot of beam polarization as a function of neutron time of flight. Bottom: Neutron transmission data for an unpolarized ^{3}He spin filter cell and a polarized cell. The chopper cutoff is completed just below 35-ms time of flight.

effects, the array was also designed to deliver sufficient spatial and angular resolution, high efficiency, and large solid angle coverage [49]. Because of the small size of the asymmetries and the proposed measurement accuracy, the average rate of neutron capture and the corresponding γ rate in the detectors must be high to keep the run time reasonable. The γ rate into a single detector averaged over the neutron time-of-flight frame from the spallation source was about 10 MHz, with the instantaneous rates much higher. Hence, and for a number of other reasons discussed in Ref. [49], the detector array uses current mode γ detection. Current mode detection is performed by converting the scintillation light from CsI(Tl) detectors to current signals using vacuum photodiodes, and the photocurrents are converted to voltages and amplified by low-noise solid-state electronics [50].

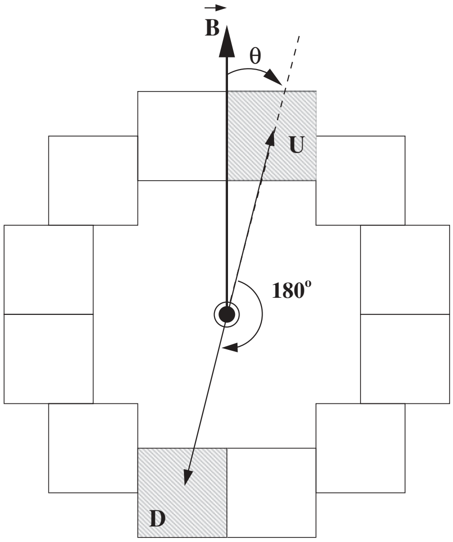

FIG. 4. A ring of 12 detectors and one up-down pair, as seen with the beam direction into the page. $\vec{B}$ is the magnetic holding field defining the direction of the neutron polarization.

IV. ASYMMETRY DEFINITION

For a vertical polarization and holding field, the PV asymmetry manifests itself as a difference in the number of photons emitted up or down with respect to the neutron polarization. A separate asymmetry is calculated for each pair of opposite detectors, as shown in Fig. 4. For a point target and a detector array with perfect spatial resolution, the measured γ-ray angular distribution would be proportional to the total detector yield $Y = 1 + A_{\gamma,\mathrm{UD}} \cos\theta + A_{\gamma,\mathrm{LR}} \sin\theta$, where θ is the angle between the neutron polarization and the momentum of the emitted photon and $A_{\gamma,\mathrm{UD}}$ and $A_{\gamma,\mathrm{LR}}$ are the PV up-down (UD) asymmetry and the parity-conserving left-right (LR) asymmetry, respectively. However, the relationship between the basic expression for the γ-ray yield and the measured asymmetry is complicated by a number of small neutron energy-dependent effects, discussed here.

The measured (raw) asymmetry ($A^{j,p}_{\mathrm{raw}}$) for each detector pair and neutron energy can be extracted in the usual way:

$$A^{j,p}_{\mathrm{raw}}(t_i) = \frac{\sum_{\uparrow}[U(t_i) - D(t_i)] - \sum_{\downarrow}[U(t_i) - D(t_i)]}{\sum_{\uparrow}[U(t_i) + D(t_i)] + \sum_{\downarrow}[U(t_i) + D(t_i)]}, \quad (7)$$

where $U(t_i)$ and $D(t_i)$ are the detector yields for the up and down detectors in a pair as defined in Fig. 4. To suppress first- and second-order detector gain drifts [60], we used the spin rotator to impose a (↑↓↓↑↓↑↑↓) neutron spin state pattern on a pulse-by-pulse basis, and raw asymmetries were formed from all valid sequences of eight beam pulses with this pattern. The corresponding physics asymmetry for a given detector pair p, spin sequence j, and ith neutron time-of-flight bin is then given by

$$A^{j,p}_{\mathrm{UD}}(t_i)\langle G_{\mathrm{UD}}(t_i)\rangle + A^{j,p}_{\mathrm{LR}}(t_i)\langle G_{\mathrm{LR}}(t_i)\rangle = \frac{\left(A^{j,p}_{\mathrm{raw}}(t_i) - A^{p}_{g} A_{f}(t_i) - A^{p}_{\mathrm{noise}}\right)}{P_n(t_i)\Delta_{\mathrm{dep}}(t_i)\Delta_{sf}(t_i)}. \quad (8)$$

On the left side of the equation, $\langle G_{\mathrm{UD}}(t_i)\rangle \simeq \cos\theta$ is the neutron energy and detection efficiency weighted spatial average detector cosine (up-down asymmetry) with respect to the (vertical) neutron polarization, $\langle G_{\mathrm{LR}}(t_i)\rangle \simeq \sin\theta$ is the detector sine (left-right asymmetry), and $A^{j,p}_{\mathrm{UD}}(t_i)$ and $A^{j,p}_{\mathrm{LR}}(t_i)$ are the physics asymmetries.

All quantities on the right-hand side of Eq. (8) as well as $\langle G_{\mathrm{UD}}(t_i)\rangle$ and $\langle G_{\mathrm{LR}}(t_i)\rangle$ are either measured or simulated. A^p_g is the gain asymmetry between the detectors in a pair, $A_f(t_i)$ is the asymmetry from pulse-to-pulse beam intensity fluctuations (see Sec. V), $P_n(t_i)$ is a correction factor owing to the neutron beam polarization, $\Delta_{\mathrm{sf}}(t_i)$ is a correction factor for the neutron spin-flip efficiency and $\Delta_{\mathrm{dep}}(t_i)$ is a correction factor for the neutron depolarization in the target. The detector-target geometry corrections $\langle G_{\mathrm{UD}}(t_i)\rangle$ and $\langle G_{\mathrm{LR}}(t_i)\rangle$ were obtained from simulations and detector motion measurements in which effective locations of the detectors were measured by moving the entire detector perpendicular to the beam and measuring the corresponding signal changes in the individual detectors.

Asymmetries were measured for 55 neutron energies between approximately 2 and 16 meV, with an energy resolution varying over this range of $\simeq$0.2 to 1.0 meV per time bin. The measured asymmetry contains contributions from background, and therefore $A^{j,p}_{\mathrm{UD}} = A^{j,p}_{\mathrm{UD,H}} + \epsilon A^{j,p}_{\mathrm{UD,b}}$ and $A^{j,p}_{\mathrm{LR}} = A^{j,p}_{\mathrm{LR,H}} + \epsilon A^{j,p}_{\mathrm{LR,b}}$, where the subscripts H and b indicate the hydrogen and background asymmetries, respectively. The background asymmetries and the relative background signal level (ϵ) were determined in auxiliary measurements and simulations (see Ref. [57] for the asymmetry measurements). The background was dominated by neutron capture on aluminum and the average level and measured asymmetry are listed in Table II.

The detector pair physics asymmetries in Eq. (8) can then be combined in error weighted averages over the neutron time-of-flight spectrum to form a single asymmetry for each detector pair in the array, for a single eight-step sequence of beam pulses. If beam intensity levels are sufficiently stable over the measurement time, these sequence asymmetries can be histogrammed for each pair. Typical run lengths were $\simeq$8.3 min and included 10 000 beam pulses or 1250 eight-step sequences and the asymmetry measurements performed usually extended over several hundred runs.

V. PERFORMANCE DIAGNOSTICS AND SYSTEMATIC EFFECTS

The performance of the experiment and apparatus was established in an extensive series of auxiliary measurements conducted prior to and during production data taking. We refer the reader to the several individual papers in the references for details that document this work. These measurements included asymmetry measurements on various materials with which the neutrons could interact, noise (beam off) asymmetry measurements, target-empty and target-out background measurements, and noise root-mean-square (RMS) width measurements. We conducted a detailed analysis of all known systematic effects that could potentially cause a false asymmetry. There are potentially several sources of false asymmetries that could mask the desired PV asymmetry we seek to measure. These false asymmetries may arise in two ways: (1) interference in the detector electronic signals correlated with the spin state of the neutrons, owing (for example) to effects from the spin rotator magnetic field, and (2) physical interactions of the polarized neutrons within the experiment and the subsequent interactions of the corresponding reaction products. A combination of measurements, published full calculations, and conservative estimates was used to estimate or bound the size of these effects. We report on the most important systematic effects here and summarize the resulting false asymmetries in Table II. General quantities that show the operational performance of the experiment are listed in Table I.

TABLE I. Statistical and systematic parameters. List of the main experimental quantities relating to the performance and efficiency of the experiment. Quantities are shown as measured (M) or estimated (E). Data runs accepted for asymmetry analysis must possess an operational apparatus (i.e., no DAQ problems, ^{3}He polarized, all detectors running, spin rotator running, and target full of parahydrogen) and a proton beam current on the spallation target of $\gtrsim$50 μA.

No. of good 8.3-min runs	4966	
Average beam current	(87 ± 6) μA	M
Average neutron polarization	$(53 \pm 2.5)\%$	M
Average spin-flip efficiency	$(98.0 \pm 0.8)\%$	M
LH$_2$ para fraction	$(99.98 \pm 0.05)\%$	M
Spin-flip scattering	2%	E/M
Average aluminum background	25%	M
Data loss from wrong spin seq.	$\approx$1.0%	M
Data loss from beam cuts	$\approx$0.5%	M

The solid target asymmetry measurements verified that possible asymmetries from materials other than LH$_2$ are below the level of accuracy achieved in this experiment. The results of these measurements are reported elsewhere [57], but we discuss the case of aluminum in detail, as neutron capture on this material produced the largest background signal in the detectors. The beam-off noise asymmetry was measured twice, once before the installation of the experiment, when the detectors had not yet been exposed to the beam, and once directly after the experiment, to verify that there was no false asymmetry contribution from electronic and magnetic pickup. The pedestal asymmetry, which includes detector signals from radiative and β decay of nuclei after the beam was turned off (shutter closed), was monitored throughout the experiment. We report on the results of these measurements here.

Noise width and background measurements were used to establish how close the observed noise is to the limit set by neutron counting statistics. This requires separate determination of γ counting statistics (i.e., the performance of the detector array) and neutron counting statistics. Determination of the latter is far more challenging, as it requires knowledge of absolute neutron flux on the LH$_2$ target and backgrounds.

A. Backgrounds

We determined the background using a combination of target-empty and target-out runs and Monte Carlo simulations. In the analysis we have made the assumption that the signal to prompt the neutron background ratio is constant over time during steady-state running. Because the LH$_2$ target density

TABLE II. False asymmetries. List of all identified sources of "false" asymmetries (those not caused by γ from neutron-proton capture), the physical process that gives rise to asymmetry, the corresponding Cartesian invariant, and the estimated (E), measured (M), or calculated (C) size. The Cartesian invariants are functions of the incoming and outgoing neutron momenta k_i, k_f, neutron spin s_n, γ-ray circular polarization p_γ, and other momenta k of the indicated reaction products. Asymmetries from prompt γ-ray emission after neutron capture (other than on hydrogen) were measured on Al, Cu, and In and are given in Ref. [57].

Description	Process	Invariant	Size	
Stern-Gerlach	$\mu \cdot \nabla B$	$\mu \cdot \nabla B$	8×10^{-11}	E
Mott-Schwinger	$\vec{n} + p \rightarrow \vec{n} + p$	$s_n \cdot k_i \times k_f$	6×10^{-9}	C/M
PA left-right	$\vec{n} + p \rightarrow d + \gamma$	$k_\gamma \cdot s_n \times k_i$	7×10^{-10}	C
γ-ray circ. polarization	$\vec{n} + p \rightarrow d + \vec{\gamma}$	$k_n \cdot P_\gamma$	7×10^{-13}	E
β decay in flight	$\vec{n} \rightarrow e^- + p + \bar{\nu}$	$s_n \cdot k_\beta$	3×10^{-11}	E
Radiative β decay	$\vec{n} \rightarrow e^- + p + \bar{\nu} + \gamma$	$s_n \cdot k_\gamma$	2×10^{-12}	E
Capture on ^{6}Li	$\vec{n} + {}^6\text{Li} \rightarrow {}^7\text{Li}^* \rightarrow \alpha + T$	$s_n \cdot k_\alpha$	2×10^{-11}	E
^{28}Al β decay, external	$\vec{n} + {}^{27}\text{Al} \rightarrow {}^{28}\text{Al} \rightarrow {}^{28}\text{Si} + e^-$	$s_n \cdot k_\beta$	1.0×10^{-8}	E
^{28}Al β decay, internal	$\vec{n} + {}^{27}\text{Al} \rightarrow {}^{28}\text{Al} \rightarrow {}^{28}\text{Si} + e^-$	$s_n \cdot k_\beta$	1.9×10^{-10}	E
^{28}Al prompt γ rays	$\vec{n} + {}^{27}\text{Al} \rightarrow {}^{28}\text{Al} + \gamma's$	$s_n \cdot k_\gamma$	$(-0.8 \pm 2.8) \times 10^{-7}$	M

variations (bubble formation or pressure oscillations) were well below the 1% level over the course of data runs in steady-state mode and are slow compared to the time span of the eight-step spin sequence, this assumption is accurate enough for our analysis. The material activation levels were monitored in the 6-ms pedestal period at the end of each neutron pulse and were seen to increase very slowly over the running period, eventually reaching a steady state. This is because the background was dominated by aluminum activation, which has a short half-life (see the following). The background levels were the same in all detectors of a given ring, with background generally decreasing toward the back of the array as expected.

Because the filled target scatters a large fraction of the neutron beam and increases the number of neutrons that can be captured in the aluminum target vessel and the aluminum cryostat vacuum windows, the true size of the background signal cannot be determined simply by a subtraction of target-full and target-empty data. A combination of measurements and Monte Carlo modeling has shown that the majority of the background signal comes from the aluminum target windows (75%), and the rest from the target vessel walls (25%). This assessment is supported by the pedestal detector signals from the portion of the frame during which the chopper blocks the beam. A decay in both pedestal level and RMS width was observed in short and long pedestal runs after a period of production running (see Fig. 5). The activation seen immediately after closing the shutter was almost entirely from aluminum, as the half-life in the observed decay is about 2.4 min, corresponding to the half-life of ^{28}Al. Using the known value for the detector gain and light yield, we were able to establish that the observed RMS width in the early pedestal signal is roughly consistent with that produced by an ≈2-MeV γ ray. The reaction $^{28}\text{Al} \rightarrow {}^{28}\text{Si}^* + e^- + \bar{\nu} \rightarrow {}^{28}\text{Si} + \gamma$ produces a 1.79-MeV γ ray. For longer periods after shutter closure, we observed a more complicated decay curve with a lower overall amplitude (see Fig. 5, bottom). This suggests that during steady-state running we have a large component of aluminum background and a smaller component of other materials with longer half-lives. Obvious candidates are the materials in the γ detector array such as ^{128}I (half-life of ≈25 min) and $^{134\text{m}}$Cs (half-life of ≈3 h).

Note that the majority of the background signal comes from the prompt radiative decay of the compound ^{28}Al nucleus before it β decays. However, this prompt signal is no longer present during the pedestal runs. The preceding analysis therefore identified only the dominant source of the background, and not its absolute magnitude. We were able to verify that the dominant background contribution comes from neutron capture on aluminum using additional auxiliary measurements with additional aluminum in the beam. We then used MCNPX simulations to infer a background-to-(hydrogen) signal ratio of 25%, when averaged over all detectors.

B. γ-ray counting statistics

In current mode detection, the counting statistics resolution is indicated by the RMS width in the sample distribution. For our detector array this width is dominated by fluctuations in the number of electrons produced at the photocathode of the vacuum photodiode, which in turn is dominated by γ-ray counting statistics when the beam is on. During beam-on measurements, the shot noise RMS width is then given by [58]

$$\sigma_{I_{\text{shot}}} = \sqrt{2qI}\sqrt{f_B}, \tag{9}$$

where q is the amount of charge created by the photocathode per detected γ ray, I is the average photocurrent per detector, and f_B is the sampling bandwidth, set by the -ms time bin width in the time-of-flight spectrum [49,59]. Figure 6 shows the RMS width for a typical detector as seen in the DAQ output. The width from counting statistics is compared to the RMS width seen for a beam-off pedestal run.

Using the known gain and efficiency (q) of the detectors, the measured average current (I), and the measured RMS width in the signal $\sigma_{I_{\text{shot}}}$, we were able to establish that the detector signal RMS was only 15% greater than that expected from γ-ray counting statistics. Figure 6 indicates that the vast

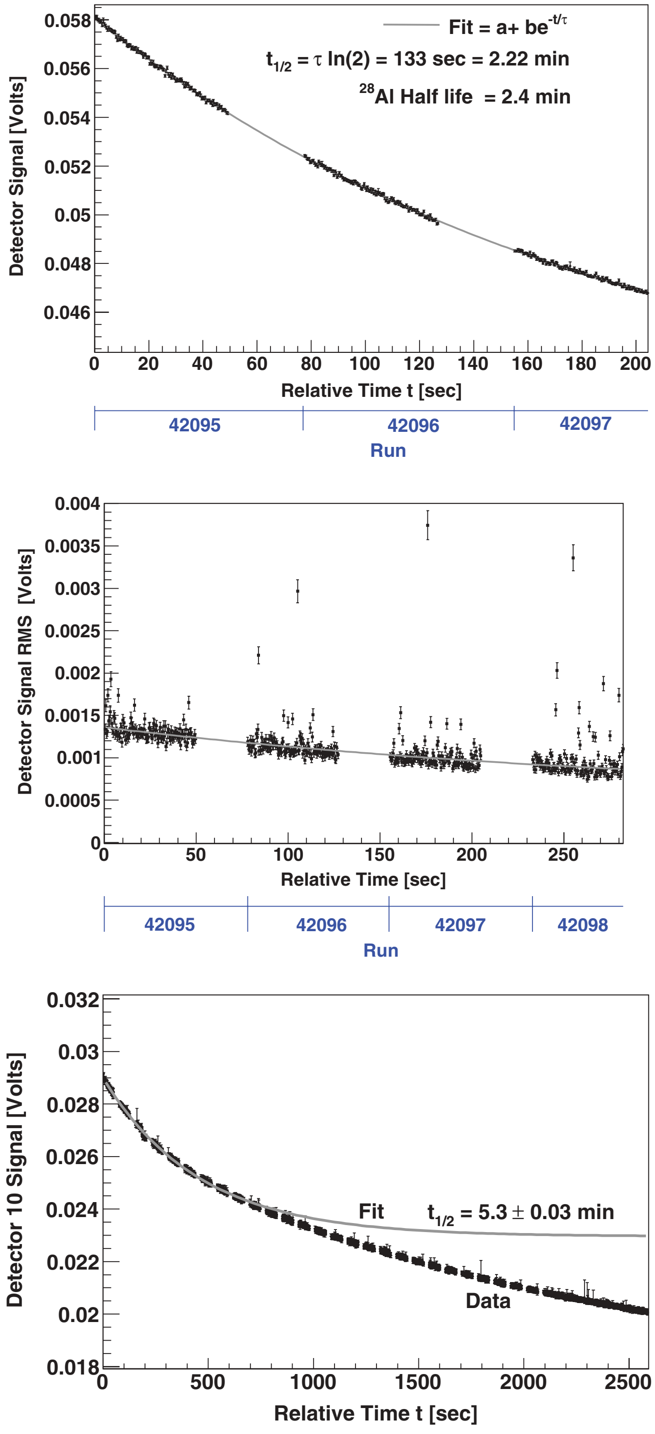

FIG. 5. (Color online) Top: Decay of pedestal mean immediately after shutter close (beam off), showing only ^{28}Al activation. Middle: Pedestal RMS decay width. Lower: Decay of pedestal mean, from runs taken longer after shutter closure, indicates a more complicated activation, resulting in a smaller signal with a longer half-life. Steady-state pedestal levels were roughly between 20 and 40 mV, depending on the detector.

majority of the 15% increase in signal RMS is caused by fluctuations in the background signals, as the noise RMS width (the only other contribution to the overall RMS width) is so small.

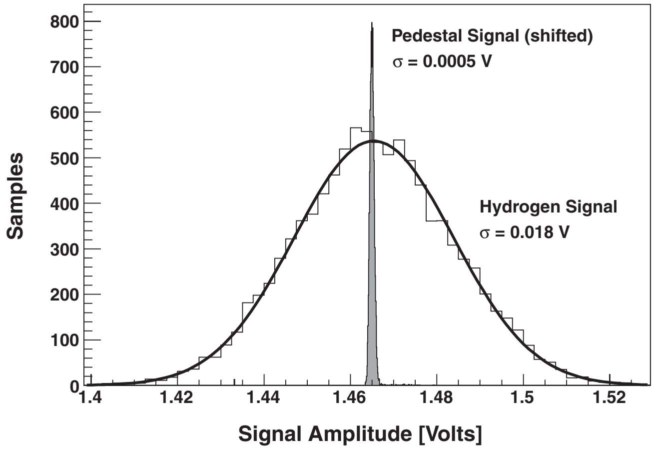

FIG. 6. γ-ray counting statistics analysis for a typical detector module. The RMS width for the beam-on signal is compared to the width seen in pedestal runs. A fit to the beam-on data histogram with an LH$_2$ target shows an RMS width of 18.4 ± 0.13 mV.

The detector signal is dominated by γ's from neutron capture in parahydrogen and aluminum. The 25% background from aluminum capture γ's increases the average current (I) more than it increases the charge quantum (q) and therefore decreases the measured (uncorrected) uncertainty, which goes as $\approx\sqrt{2q}/\sqrt{I}$. To extract the hydrogen uncertainty given the measured RMS width, which has contributions from both hydrogen and aluminum capture γ's, we must therefore apply Eq. (9) and use our estimate of the fraction of the signal from the aluminum background to regress out the hydrogen contribution.

C. Beam asymmetries

Within each pulse the neutron flux is neutron energy dependent (see Fig. 2) and varies slightly from pulse to pulse. However, this variation is not correlated with the neutron spin state. The beam flux is measured with the beam monitors and a single spin sequence step with an anomaly, such as a transient spike or dip in the signal, could produce a nonzero raw asymmetry. This can happen in combination with a nonzero detector gain asymmetry if the change in flux is real rather than electronic [see Eq. (8)]. The RMS width in the beam asymmetry, when histogrammed over the entire data set, is $\sigma_f \simeq 10^{-3}$. The gain asymmetry was monitored throughout the experiment for all detectors and is $A_g^p \simeq 10^{-3}$. Spin sequence asymmetries are combined in error weighted averages to form an asymmetry for a given run (see Sec. IV). If the anomalous sequence asymmetry is large or if several of them occur in the same run, then a nonzero run asymmetry is generated. Therefore we placed a cut on sequences and runs with high beam asymmetries. This cut was implemented if any one spin step pulse had a current that was more than 1.5σ from the average over all pulses in an eight-step sequence. Within any given spin sequence, the maximum observed product gain beam asymmetry was of order 10^{-6}, whereas the typical raw asymmetry values were of order 10^{-5}. In addition, as reversal of the neutron polarization happens downstream of the spallation source and the detector gain is not correlated with the spin rotator state [49], the beam-gain product asymmetry has random signs with respect to the raw asymmetry and averages to 0. The number of lost spin sequences owing to the beam asymmetry cut was very small and the amount of corresponding data loss was only about 0.5%.

D. Pedestal asymmetries

For each spin sequence a pedestal asymmetry was calculated from the portion of the neutron pulse after chopper cutoff. The measured pedestal asymmetry was $(-3.5 \pm 3.0) \times 10^{-9}$, consistent with 0. This pedestal analysis was indiscriminate in the sense that no filtering was conducted to remove transient spikes in the data or other large outlier events. In addition to the pulse portion after chopper cutoff all separate pedestal runs were included as well. The time required to measure the pedestal asymmetry to 5×10^{-9} was equivalent to approximately 30 h of continuous data taking [49] with the neutron beam.

E. False asymmetries

The primary technique for isolating the parity-odd signal and reducing possible false asymmetries generated by gain nonuniformities, slow efficiency changes, beam fluctuations, and fluctuations in the target thickness is frequent neutron spin reversal on a time scale short compared to drift rates or fluctuation periods. Spin reversal allows asymmetry measurements to be made in each spin state for any pair of opposing detectors in a ring (Fig. 4) and for consecutive pulses with different spin states, thereby greatly suppressing the sensitivity of the measured asymmetry to detector gain differences, drifts, and intensity fluctuations. By choosing the eight-step sequence of spin reversal described in Sec. IV, the linear and quadratic components of time-dependent detector gain drifts in a sequence can be greatly suppressed [60]. To achieve neutron spin reversal the experiment employed a radio-frequency resonant neutron spin rotator (RFSR) [61] which operates at 29 kHz for the 1 mT guide field. The neutron spin direction is reversed when the RFSR is on and is unaffected when it is off. The spin-flip efficiency averaged over the beam cross section (5-cm radius) was measured to be 98.0% [61].

Possible false asymmetries of electronic origin without neutron beam may be measured in two ways. The first type occurs when there exists a coupling between the detector preamplifier circuit and the electronics used to switch the RFRS magnetic field on and off. The resulting effect would appear as an addition to (i.e., reside on top of) the detector signal. This contribution was investigated by running the spin rotator electronics together with the detector array and DAQ and looking for a spin-correlated signal in the detectors [61]. The second type of asymmetry occurs when the magnetic field from the spin rotator leaks into the vacuum photodiodes of the γ-ray detectors and changes their gain. This effect was suppressed by enclosing the radio-frequency fields of the spin rotator in an aluminum can and investigated experimentally by running the spin rotator with the field on together with the detector array. For this test the bias signals in the detectors were produced by illuminating the detector crystals with light emitting diodes [49].

Possible false asymmetries owing to spin state correlated electronic pickup and possible radio-frequency magnetic field induced gain changes in detector vacuum photodiodes have been measured previously and are consistent with 0 to within 5×10^{-9} [49]. Note also that the measured pedestal asymmetry of $(-3.5 \pm 3.0) \times 10^{-9}$ mentioned earlier would include the product of both of these effects, in addition to possible asymmetries from neutron induced nuclear decay in materials other than hydrogen. Except for prompt γ rays emitted immediately after neutron capture, from the compound nuclear decay, all other asymmetries from subsequent nuclear decay would show up in the pedestal asymmetry.

To analyze the large number of possible false asymmetries arising from polarized neutron interactions other than the reaction with parahydrogen, we made a list of Cartesian invariants involving the neutron spin and other possible kinematic variables, such as the momenta and spins of the reaction products (see Table II), and analyzed all physical processes that involve these correlations and can generate a signal in the γ detectors. We briefly describe the most important processes and estimate their sizes here. The various sizes of all systematic effects from calculations and measurements are listed in Table II.

1. Stern-Gerlach steering

Spin-state-correlated Stern-Gerlach steering of the neutrons between the spin rotator and the target can generate a false up-down asymmetry. The Stern-Gerlach force is $\vec{F} = \vec{\mu} \cdot \vec{\nabla}\vec{B}$, where $\vec{\mu}$ is the neutron magnetic moment. If there is a magnetic field gradient along the direction of the guide field, the Stern-Gerlach force moves the beam along the direction of the neutron magnetic moment and its sign changes as the neutron spin is flipped to produce an apparent parity-odd asymmetry signal in the detector array. The resulting false asymmetry can be reduced to below the accuracy of the PV asymmetry measurement by exploiting the fact that the Stern-Gerlach force is small and by keeping the field gradient in the experimental region small. We employed a stable guide field with a vertical strength of $B = 1$ mT and a vertical field gradient $dB_y/dy < 1\ \mu\text{T/cm}$. We measured the magnetic field gradient to be less than $0.2\ \mu\text{T/cm}$. The displacement of the neutron beam assuming this gradient over the 0.5-m distance between the spin rotator and the target is $\Delta y = 0.6 \times 10^{-11}$ m for a neutron energy of 10 meV. The corresponding false asymmetry, given the distance of $r = 0.3$ m from the center of the stopping distribution in the target to the detector, is approximately $2\Delta y/r = 0.8 \times 10^{-10}$, which is very small compared to the statistical uncertainty. The requirement for small field gradients drove our decision to use a resonant spin rotator rather than an adiabatic spin rotator, which possesses a field gradient.

2. PV γ-ray asymmetry from neutron capture on aluminum

From measurements of detector signals when the target was empty and with additional aluminum added in front of the target, we were able to estimate that 7% of the incident neutrons captured on aluminum (mainly in the target windows). The γ decay of the capture state in ^{28}Al can yield an asymmetry if the states of ^{28}Al have mixed parity. In Ref. [57] the authors calculate the RMS value of the asymmetry to be 1.3×10^{-7} in the framework of the statistical model of the compound nucleus and report the measured size of the asymmetry to be $(-0.02 \pm 3) \times 10^{-7}$ based on measurements taken before the hydrogen data run. Analysis of additional data taken during the hydrogen production run with the target empty improved the accuracy of the ^{28}Al asymmetry measurement to $(-0.8 \pm 2.8) \times 10^{-7}$. As discussed in Sec. V A, during production running with hydrogen the majority of the detector signal is a combination of signals obtained from neutron capture in hydrogen, $\vec{n} + p \to d + \gamma$ (75%), and on aluminum, $\vec{n} + {}^{27}\text{Al}^* \to {}^{28}\text{Al} + \gamma$'s. The background signal gives a correction to the central value of the asymmetry. The measured hydrogen γ-ray asymmetry after background correction is

$$A_p = \frac{A_{\text{raw}}(Y_p + Y_{\text{bgr}}) - A_{\text{bgr}} Y_{\text{bgr}}}{Y_p} = A_{\text{raw}}(1 + \epsilon) - A_{\text{bgr}}\epsilon, \tag{10}$$

where A_{raw} is the measured (uncorrected) asymmetry and A_{bgr} is the measured background asymmetry. The quantity $\epsilon = (Y_{\text{bgr}}/Y_p)$ is the fractional background yield, where Y_p and Y_{bgr} are the γ-ray yields from hydrogen and aluminum runs, respectively. ϵ varies across the detector rings but is constant within each ring. Averaging over the detector array gives $\epsilon \simeq 0.33$. The uncertainty in the background correction also increases the statistical uncertainty in the extracted $\vec{n} + p \to d + \gamma$ asymmetries. The statistical uncertainty in A_p is given by

$$\sigma_p = \sqrt{(1+\epsilon)^2 \sigma_{\text{raw}}^2 + \epsilon^2 \sigma_{\text{bgr}}^2}, \tag{11}$$

where σ_{raw} and σ_{bgr} are the statistical uncertainties in A_{raw} and A_{bgr} respectively.

3. *Bremsstrahlung*

Bremsstrahlung created by β electrons is a possible source of false asymmetries. Both internal and external bremsstrahlung processes create photons that deposit energy in the detectors that is correlated with the neutron spin direction. In the NPDGamma experiment, we have to consider the bremsstrahlung induced photon production from free neutron β decay in the beam before capture as well as the β decay of the ^{28}Al ground state after initial γ-ray de-excitation. In both cases the direction of the electron is correlated with the neutron spin direction. We consider external bremsstrahlung, in which the β electron produces photons as it moves through material after decay, and we consider internal bremsstrahlung, in which the β electron is deflected by its own associated nucleus. One would expect that the false asymmetries produced by bremsstrahlung are small because only a small fraction of the decay energy is converted into photons. However, the asymmetry from external bremsstrahlung owing to ^{28}Al is only about an order of magnitude smaller than the theoretically predicted size of the PV $\vec{n} + p \to d + \gamma$ asymmetry. We therefore present our estimate for the size of this effect in more detail.

For free neutron β decay, the neutron spin-electron correlation coefficient is $A_{s_n,k_\beta} = -0.117$ [62]. Only 2.7×10^{-7} of the 10-meV neutrons decay before stopping in the hydrogen target. Some of the energy of the β electron is converted into photons via bremsstrahlung in the material it passes through, or the β electron emits bremsstrahlung photons after being deflected by the electric field of its own nucleus. In both cases the photons deposit energy in the γ detector and produce a signal correlated with the neutron spin direction. The aim of our analysis is to estimate the size of this correlation and use it to calculate limits for a possible false asymmetries associated with these effects.

In the decay of the compound ^{28}Al nucleus, the correlation with the initial neutron spin direction is complicated by both the angular momentum transitions in the electromagnetic decay and the fact that the half-life of ^{28}Al is large compared to the neutron spin reversal. Both of these effects reduce the correlation, but the number of neutrons that capture on aluminum is much larger than the number of free (in-beam) neutron decays. The ground-state spin of ^{27}Al is 5/2. The *s*-wave capture state in ^{28}Al can therefore have an angular momentum of 2 or 3 and is polarized. We calculated the population of the magnetic substates of the capture state by expressing the capture amplitude as the product of a reduced matrix element and a vector-coupling coefficient [63]. The capture state decays to the ground state of ^{28}Al by emission of four γ rays on average, which reduce the polarization by carrying away angular momentum. We modeled the γ decay process by assuming either three, four, or five transitions. The multipolarity of all but the last transition was assumed to be 1 and the last was assumed to be the minimum L necessary to satisfy the triangle inequality for the $J = 3$ ^{28}Al ground state. The transition rates between magnetic substates were also calculated according to Ref. [63]. The estimated polarization of the ^{28}Al ground state is 0.16 ± 0.03. The uncertainty is taken to be the range of the calculated values.

The lifetime of the ^{28}Al ground state is 138.6 s, much longer than the 50-ms neutron pulse width used in this experiment. Therefore the reversal rate of ^{28}Al polarization is considerably lower than the reversal rate of the eight-step spin sequence from which the $\vec{n} + p \to d + \gamma$ asymmetry is calculated. In addition, the ^{28}Al polarization is reduced by interaction with the fluctuating magnetic field of the conduction electrons. The polarization is reduced by a factor of 6×10^{-5} if the spin-lattice relaxation is neglected and by 2.5×10^{-6} if a spin-lattice relaxation time of 6 ms is assumed. If we neglect spin-lattice relaxation the ^{28}Al polarization is reduced to about 10^{-5} on average.

In order to calculate the size of the possible γ-ray asymmetries, it is also necessary to understand the modification of the correlation between the photon direction and the neutron spin direction. This correlation depends on the initial direction of the β electron and the correlation between the electron direction and the photon direction. We assume that an electron has an initial angular distribution with respect to the neutron spin direction, given by $1 + A\beta \cos(\vartheta_{\vec{s}_n \cdot \vec{k}_\beta})$, where A is the neutron β asymmetry coefficient, and $\beta = v_e/c$, and $\vartheta_{\vec{s}_n \cdot \vec{k}_\beta}$ is the angle between the neutron spin direction and the momentum of the emitted β. If the photon distribution with respect to the electron direction is azimuthally symmetric and $P(\vartheta_{\vec{k}_\beta \cdot \vec{k}_\gamma}, E_\gamma, T_\beta)$ is the probability for photon emission with a given angle and energy, for a given electron energy, then the energy-weighted value of the γ asymmetry coefficient is

$$\langle A_\gamma E_\gamma \rangle = A\beta \int dE_\gamma \int d\cos\left(\vartheta_{\vec{k}_\beta \cdot \vec{k}_\gamma}\right) \frac{E_\gamma}{2} \cos\left(\vartheta_{\vec{k}_\beta \cdot \vec{k}_\gamma}\right) \times P\left(\vartheta_{\vec{k}_\beta \cdot \vec{k}_\gamma}, E_\gamma, T_\beta\right).$$

Internal bremsstrahlung was first approximately calculated by Bloch [64] and later by Chang and Falkolff [65]. The β decay probability has the form of a conditional probability. The free neutron or the ^{28}Al nucleus initially β decays according to

$$\frac{d^2\Gamma}{d\Omega_e dW_e} = \rho(W_e)\left(1 + A\beta \cos\left(\vartheta_{\vec{s}_n \cdot \vec{k}_\beta}\right)\right),$$

where $\rho(W_e)$ is the energy spectrum of the β electrons. A photon is produced at an angle $\vartheta_{\vec{k}_\beta \cdot \vec{k}_\gamma}$ with respect to the electron direction and with an energy of E_γ. So we obtain

$$\frac{d^4\Gamma}{d\Omega_e dW_e d\Omega_\gamma dE_\gamma} = \rho(W_e + E_\gamma)\left(1 + A\beta \cos\left(\vartheta_{\vec{s}_n \cdot \vec{k}_\beta}\right)\right) \frac{d^2\Phi}{dE_\gamma d\Omega_\gamma}$$

and

$$\frac{d^2\Phi}{dE_\gamma d\Omega_\gamma} = \frac{\alpha E_\gamma}{4\pi^2}\left(\frac{2W_e^2 + 2W_e E_\gamma + E_\gamma^2}{W_e(W_e + E_\gamma)\left[1 - \beta\cos\left(\vartheta_{\vec{k}_\beta \cdot \vec{k}_\gamma}\right)\right]} - \frac{1}{W_e^2\left[1 - \beta\cos\left(\vartheta_{\vec{k}_\beta \cdot \vec{k}_\gamma}\right)\right]^2} - 1\right).$$

These expressions can be integrated with respect to E_γ, Ω_γ, W_e, and Ω_e to obtain an energy weighted value of the asymmetry $\langle A_\gamma \rangle = \langle E_\gamma \cos(\vartheta_{\vec{s}_n \cdot \vec{k}_\beta}) \rangle$.

In external bremsstrahlung a small fraction of the electron energy is emitted as bremsstrahlung photons. As the electron slows down, its direction is changed by the multiple scattering from the screened Coulomb field of the nuclei in the stopping medium. If the initial distribution of electron directions is $1 + A_i \beta \cos(\vartheta_{\vec{s}_n \cdot \vec{k}_\beta})$, then after a single scattering event owing to an azimuthally symmetric process, the asymmetry is reduced by averaging

$$A' = A \frac{\int \frac{d\sigma}{d\Omega} \cos(\theta) d\Omega}{\int \frac{d\sigma}{d\Omega} d\Omega}.$$

For a thick layer of scattering centers the asymmetry is reduced by multiple scattering by a factor $\Phi(E_i, E_f)$, given by

$$A_f = A_i \Phi(E_i, E_f) = A_i e^{-\frac{dN}{dx}(\int_0^x dx \int \frac{d\sigma}{d\Omega} \cos(\theta) d\Omega)} = A_i e^{-\frac{dN}{dx}(\int_{E_i}^{E_f} dE \int \frac{d\sigma}{d\Omega} (\frac{dE}{dx})^{-1} \cos(\theta) d\Omega)}.$$

We evaluated $\Phi(E_i, E_f)$ for the Thomas-Fermi-Moliere form factors given by Tsai [66] and for the standard approximation for multiple scattering given by the Particle Data Group. Results from these two procedures agreed to within 4%. The energy weighted correlation between the neutron spin direction and the bremsstrahlung photons for a fully polarized nucleus is

$$\langle C_{\Delta E} \rangle = \int_0^{Q_\beta} \beta(E)\rho(E) dE \int_0^E dE' f_{\mathrm{rad}}(E') \times \left\langle \cos\left(\vartheta_{\vec{k}_\beta \cdot \vec{k}_\gamma}\right) \right\rangle \Phi(E, E'),$$

where

$$f_{\mathrm{rad}} = \frac{\left(\frac{dE}{dx}\right)_{\mathrm{rad}}}{\left(\frac{dE}{dx}\right)_{\mathrm{rad}} + \left(\frac{dE}{dx}\right)_{\mathrm{coll}}}$$

is the fraction of the differential energy loss owing to radiation and Q_β is the end-point energy. The energy loss quantities were taken from Ref. [67]. The bremsstrahlung radiation is forward peaked but is not emitted exactly parallel to the electron direction. The average value $\langle \cos(\vartheta_{\vec{k}_\beta \cdot \vec{k}_\gamma}) \rangle$ is always close to unity. In our calculations we used the semiclassical approximation for the angular distribution of photons [68], which is independent of the photon energy:

$$\frac{d\sigma}{d\Omega} \simeq \frac{[\beta - \cos(\vartheta)]^2 + [1 - \beta\cos(\vartheta)]^2}{[1 - \beta\cos(\vartheta)]^4}.$$

We evaluated $\langle C(\Delta E) \rangle$ for free neutron β decay and the decay of ^{28}Al. The reduction in the asymmetry owing to multiple scattering and the angular distribution of the bremsstrahlung is more than an order of magnitude.

The false asymmetries for internal and external bremsstrahlung are given by $A_B = \frac{Q_\beta}{E_\gamma} \langle C_{\Delta E} \rangle A f P f_{\mathrm{rev}}$ where f is the fraction of neutrons that decay or capture on ^{27}Al, A is the asymmetry, P is the polarization of the decaying state, f_{rev} is the fraction of neutrons that capture in total, and P_r is the reduction of the polarization from rapid spin reversal. The various parameters used or obtained in the calculation are reported in Table III and the resulting false asymmetries are listed in Table II. All of the false asymmetries are more than an order of magnitude smaller than the statistical uncertainty achieved in this experiment. By far the largest false asymmetry is from external bremsstrahlung from aluminum, which is reduced by a factor of 4 by multiple scattering and the angular distribution of bremsstrahlung relative to the electron direction. This false asymmetry is small compared to the statistical uncertainty in the present experiment but may be a problem in the next phase of the experiment, where the goal statistical uncertainty is 10^{-8}. Fortunately, changes in the implementation of the next phase of the experiment further reduce this systematic effect.

4. *Parity-allowed left-right asymmetries*

Two sources for parity-allowed (PA) left-right asymmetries exist: radiative capture (PA $\vec{n} + p \rightarrow d + \gamma$) and spin dependent beam centroid shifts due to the electromagnetic spin-orbit interaction of polarized neutrons with nuclei and their electron clouds (Mott-Schwinger scattering) [69]. The sum of these left-right asymmetries was measured simultaneously with

TABLE III. False asymmetries from bremsstrahlung. Factors entering into the calculations for the false γ-ray asymmetries from internal and external bremsstrahlung after β decay.

	Neutron β decay	^{28}Al β decay
Q_β/E_γ	0.35	1.27
A (electron-spin asymmetry)	−0.11	−1.0
f (fraction that participates)	2.7×10^{-7} (β decay)	0.07 (capture on ^{27}Al)
P_r (polarization reversal rate reduction)	1.0	4×10^{-4}
Pol (polarization of decaying state)	1.0	0.16
$\langle C_{\Delta E}\rangle$ (internal)	0.8×10^{-4}	3.6×10^{-4}
$\langle C_{\Delta E}\rangle$ (external)	1.2×10^{-4}	7.0×10^{-3}
$A_{\rm false}$ (internal)	3.0×10^{-11}	1.9×10^{-10}
$A_{\rm false}$ (external)	2.4×10^{-11}	1.0×10^{-8}

the up-down asymmetry using the larger sensitivity of the horizontal detector pairs to the left-right asymmetry.

PA left-right asymmetries can contaminate the PV signal through misalignment of the neutron polarization and the detector axis. Alignment of the magnetic field direction with the detector axis suffices to align the neutron spin with the detector axis, as the motion of the neutron magnetic moment in the magnetic field of the apparatus is very close to the adiabatic limit. We therefore performed a careful alignment of the detector axis with the magnetic holding field and characterized other sources of misalignment such as geometric tolerances and the spatial uniformity of the detector response.

The physical displacement of the detector elements can be estimated from the mechanical tolerances for the detector stand (1 mm) and the distance from the target center to the detectors (29 cm). The angular uncertainty for an individual detector is $\delta\phi = 3$ mrad. The homogeneity of the CsI detection medium can be estimated from detector light yield and efficiency measurements. We calibrated all our detectors using a single γ source, a single photomultiplier, and a fixed geometry. These data were used to individually match measured photodiode gains to light yields from the CsI detectors [49] before assembly of the array to make the response of the array as spatially uniform as possible. The measured light yield variation from detector to detector was $\sigma = 20\%$. The uncertainty in the location of the centroid of the response can be estimated as $\delta x \simeq \sigma L/\sqrt{12}$, where $L = 15$ cm is the side length of a CsI detector. The angular uncertainty of an individual detector is 28 mrad. The accuracy in the alignment of the fluxgate magnetometer that was used to measure the direction of the magnetic guide field was estimated to be 1° or 16 mrad. Combining these three uncertainties in quadrature gives an overall uncertainty of 32 mrad. The dominant uncertainty is correlated for all CsI detectors. Therefore the mixing of the PA left-right asymmetries into the PV up-down asymmetries is given by $A_{\rm false} = \delta\vartheta A_{\rm LR}$, with $\delta\vartheta = 32$ mrad. The PA left-right asymmetry in the reaction $\vec{n} + p \to d + \gamma$ has been calculated to be 2.3×10^{-8} at 10 meV [70]. The false asymmetry caused by mixing this left-right asymmetry into the up-down detector channel is then $\simeq 7 \times 10^{-10}$ and is therefore negligible.

The PA asymmetry from Mott-Schwinger neutron scattering shifts the centroid of the capture distribution left-right upon neutron spin flip, thereby producing a left-right asymmetry. Mott-Schwinger scattering comes from the interaction of the magnetic moment of the neutron with the motional magnetic field from the screened Coulomb field of the nucleus. The analyzing power is always negative. Mott-Schwinger scattering produces a left-right asymmetry because neutrons scatter elastically before absorption for about 50% of the events. The predicted left-right asymmetry reaches a maximum in the slow neutron energy regime of -1.8×10^{-8} for 7.5-meV neutrons. This result for the hydrogen molecule [71] corrects an earlier calculation [69] that neglected to take into account the need to express the orbital angular momentum appearing in the partial wave expansion in terms of the relative angular momentum of the neutron and the molecular center of mass. This error only affects the calculation in the molecule and not that of the RMS asymmetry from atom scattering.

Since the PA left-right asymmetry in the reaction $\vec{n} + p \to d + \gamma$ makes a negligible contribution to the systematic error, as shown, we use the observed left-right asymmetry of $(-2 \pm 2) \times 10^{-7}$ as an upper limit on the left-right asymmetry from Mott-Schwinger scattering. The observed left-right asymmetry places an upper bound on the induced false up-down asymmetry from detector misalignment of $(6 \pm 6) \times 10^{-9}$, which is still negligible for the statistical uncertainty reported in this paper.

5. Photon circular polarization

The 2.2-MeV photons from the capture of polarized neutrons on hydrogen are circularly polarized in the direction of the neutron spin. The polarization transfer coefficient has been measured to be $\gamma_{\rm CP} = 1.5 \times 10^{-3}$ [72]. About 4% of the photons from neutron capture in the target do not get stopped in the 15-cm-thick CsI detectors and are backscattered from the steel roof and floor of the experimental cave. The 6-mm-thick steel roof and floor were demagnetized in the Earth's field before installation and were weakly magnetized by the 1-mT magnetic guide field in the cave. About 0.05% of the photons are scattered back into the detectors. The backscattering cross section depends on the product of the electron polarization in the steel (S) and the photon circular polarization ($P_{C,\gamma}$):

$$\frac{d\sigma}{d\Omega} = \left(\frac{d\sigma}{d\Omega}\right)_{\rm unpol} = P_{C,\gamma} S \left(\frac{d\sigma}{d\Omega}\right)_{\rm pol}.$$

The analyzing cross section is

$$\left(\frac{d\sigma}{d\Omega}\right)_{\rm pol} = 4.1 \text{ mb/sr}.$$

The false γ-ray asymmetry can be conservatively estimated as

$$A_{\rm CP} = \gamma_{\rm CP} \frac{E_{\gamma'}}{E_\gamma} T N_{\rm Fe} P_{\rm N} \left(\frac{d\sigma}{d\Omega}\right)_{\rm pol} \Omega_{\rm det} \simeq 0.7 \times 10^{-12},$$

where $E_\gamma = 2.2$ MeV and $E_{\gamma'} = 0.24$ MeV are the energies of the incident and Compton backscattered photons, $T = 0.07$ is the transmission of the 2.2-MeV γ rays through the CsI, $P_N = 0.001$ is the number of polarized electrons per iron atom, and $N_{\rm Fe} = 5.5 \times 10^{22}$ is the number of Fe atoms per square centimeter.

6. Neutron capture on ^{6}Li

About 25% of the polarized neutrons that are not captured on the protons in the target are absorbed on the ^{6}Li-loaded neutron shielding that surrounds the target vessel. Most of the remaining neutrons are either transmitted or captured on the aluminum vessel. Neutrons that are captured on ^{6}Li undergo the reaction $\vec{n} + {}^6\text{Li} \rightarrow {}^7\text{Li}^* \rightarrow \alpha + T$. The PV directional asymmetry between the neutron spin and the momentum of the α particle, $\vec{s}_n \cdot \vec{k}_\alpha$, has been measured to be $A_{S_n\alpha} = (8.8 \pm 2.1) \times 10^{-8}$ [73]. Most of the α particles range out in the shielding material. However, with a probability $P_r \simeq 10^{-4}$, the α particles can undergo (α, n) reactions, leading to ≈20-MeV neutrons. We conservatively assume that each neutron deposits $E_{\rm dep} = 20$ MeV in the CsI detector. The upper limit of the false asymmetry can then be estimated as

$$A_{n,\rm Li} \simeq \frac{E_{\rm dep}}{E_\gamma} P_{\rm abs} P_r A_{S_n\alpha} = 1.8 \times 10^{-11}.$$

F. Spin-flip scattering and depolarization

The depolarization of neutrons via spin-flip scattering from the protons in the target as well as from the nuclei in other materials (primarily aluminum) dilutes the measured γ-ray asymmetry. For all target materials that the neutron beam can interact with, the neutron depolarization is a small effect that can be estimated to sufficient accuracy for nonmagnetic materials using the known neutron coherent and incoherent cross sections and a suitable Monte Carlo. Table IV lists the estimated spin-flip probabilities for the various materials the neutrons could capture on, as well as the corresponding calculated average correction factors $\langle \Delta_{\rm dep}(t_i) \rangle$. The degree of spin-flip scattering is neutron energy dependent and a Monte Carlo calculation for the depolarization as a function of neutron energy was applied to the data. Depolarization was

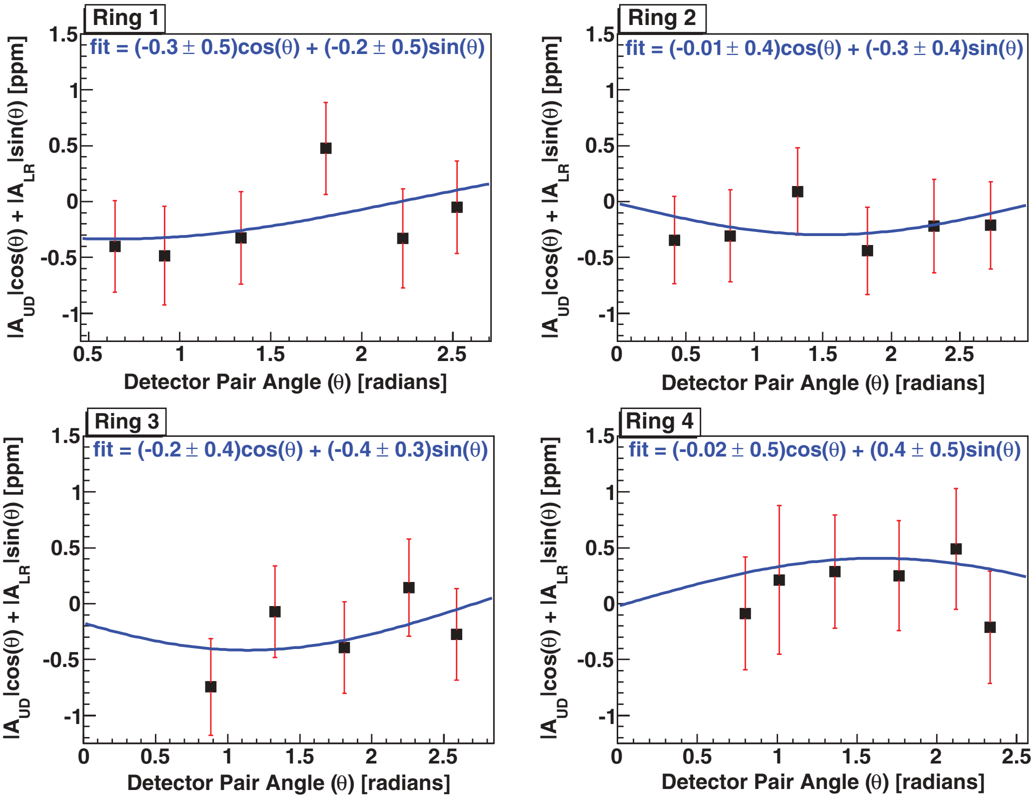

FIG. 7. (Color online) Measured asymmetry fits for each ring.

TABLE IV. Neutron depolarization. Estimates for spin-flip probability and corresponding corrections to the measured γ-ray asymmetry owing to depolarization in the materials seen by the beam. $\langle\Delta_{\rm dep}(t_i)\rangle$ is used as a correction factor in the extraction of the physics asymmetry [see Eq. (8)].

	$P_{\rm dep}\frac{2\sigma_{\rm inc}}{3\sigma_{\rm tot}}$	$\langle\Delta_{\rm dep}(t_i)\rangle$	Location
Al	3×10^{-3}	1	LH_2 target, beam monitor, and RFSF windows
Cu	2×10^{-2}	0.95	LH_2 target
In	2×10^{-3}	1	LH_2 target
B_4C	5×10^{-4}	1	Shielding

also monitored with a polarized ^{3}He cell located behind the hydrogen target. To prevent beam depolarization in the LH_2 target, it was operated with a parahydrogen fraction of 99%, as only the orthohydrogen contributes to the spin-flip scattering for neutrons energies below 15 meV.

VI. RESULTS

The raw spin sequence asymmetries calculated from Eq. (7) were averaged separately for each detector pair, with weights applied for all correction factors shown on the right-hand side of Eq. (8). As mentioned before the background levels were the same in all detectors of a given ring, with background generally decreasing toward the back of the array, downstream from the incoming beam. The measured background levels and asymmetries were applied to the six detector pair asymmetries within each ring using Eqs. (10) and (11).

The resulting measured detector pair asymmetries were plotted versus their geometry factors (effective angles) as shown in Fig. 7. The physics asymmetries for each ring were obtained from a least-squares minimization analysis and then averaged together. The final results are

$$A_{\gamma,\rm UD} = [-1.2 \pm 2.1\,(\text{stat.}) \pm 0.2\,(\text{sys.})] \times 10^{-7},$$
$$A_{\gamma,\rm LR} = [-1.8 \pm 1.9\,(\text{stat.}) \pm 0.2\,(\text{sys.})] \times 10^{-7}.$$

The large parity-odd γ asymmetry in ^{35}Cl observed in previous measurements [74,75] was used to verify that a nonzero asymmetry can be measured with our apparatus [57,76]. A target of CCl_4 was used to perform this measurement. The neutron absorption in this material is dominated by neutron absorption in ^{35}C. These results are shown in Fig. 8.

In general, the up-down and left-right asymmetries must be extracted using the fit already described. Higher-order corrections to the fitting function used here (PV or not) are introduced by higher partial waves in the expansion of the initial and final two-nucleon states representing more complicated scalar combinations between the neutron spin $\vec{s}_n$ and the outgoing γ-ray momentum direction $\vec{k}_\gamma$. For the up-down asymmetry the angular distribution is obtained from initial and final two-nucleon states with components up to the P waves producing the $\vec{s}_n \cdot \vec{k}_\gamma$ correlation. The left-right asymmetry originates from the $\vec{s}_n \cdot (\vec{k}_\gamma \times \vec{k}_n)$ correlation. PV corrections from higher partial waves are negligible because they represent a second-order perturbation proportional to the weak coupling squared. Recall that beam asymmetries are only produced if there are pulse-to-pulse fluctuations in the number of neutrons in combination with a difference in gain between a given detector pair. Neither beam fluctuations nor detector gain differences are correlated with the neutron spin, and therefore this beam-gain asymmetry does not contain any up-down or left-right dependence. Owing to the sum over the eight-step sequence, the beam-gain asymmetry averages to 0 and its root mean square width is determined by the size of beam fluctuations.

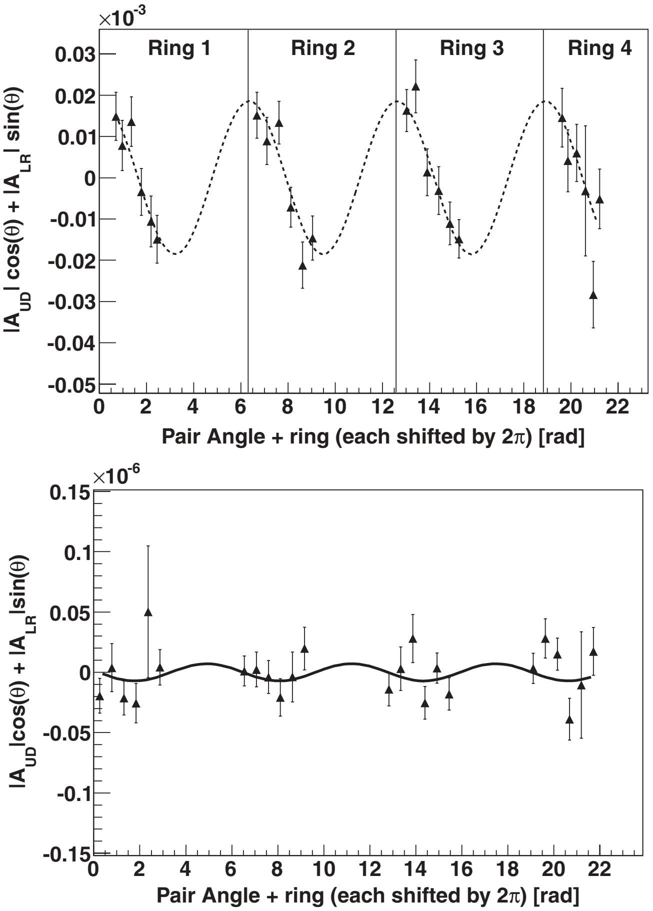

FIG. 8. Top: Measured ^{35}Cl asymmetries for each pair, plotted versus the angle of the first detector in the pair with respect to the vertical. The final asymmetry is extracted from the fit $A_{\rm UD}\cos(\theta) + A_{\rm LR}\sin\theta$, with $A_{\rm UD}$ and $A_{\rm LR}$ as fit parameters. Bottom: Asymmetries from noise measurements.

TABLE V. Statistical uncertainties for each detector ring, for the uncorrected ($A_{\rm raw}$, $\sigma_{\rm raw}$) and background ($A_{\rm bgr}$, $\sigma_{\rm bgr}$) asymmetries and the background corrected final hydrogen asymmetry (A_p, σ_p). The quantity $\epsilon = Y_{\rm bgr}/Y_p$ is the fractional background to hydrogen yield [see Eq. (10)]. For the background asymmetry and uncertainty, we used the measured aluminum asymmetry averaged over all four rings. Correction factors for beam polarization, spin-flip efficiency, and spin-flip scattering were applied before background correction.

Ring	ϵ	Direction	$A_{\rm raw}$ (ppm)	$\sigma_{\rm raw}$ (ppm)	$A_{\rm bgr}$ (ppm)	$\sigma_{\rm bgr}$ (ppm)	A_p (ppm)	σ_p (ppm)
1	0.6	UD	−0.27	0.29	−0.08	0.28	−0.38	0.49
		LR	−0.20	0.29	−0.2	0.28	−0.20	0.49
2	0.4	UD	−0.015	0.24	−0.08	0.28	0.01	0.36
		LR	−0.29	0.24	−0.2	0.28	−0.33	0.35
3	0.2	UD	−0.17	0.33	−0.08	0.28	−0.19	0.40
		LR	−0.38	0.27	−0.2	0.28	−0.42	0.33
4	0.12	UD	−0.02	0.43	−0.08	0.28	−0.013	0.48
		LR	0.41	0.40	−0.2	0.28	0.48	0.45
Combined		UD	−0.12	0.15	−0.08	0.28	−0.12	0.21
		LR	−0.23	0.14	−0.2	0.28	−0.18	0.19

A. Experimental uncertainties

The final statistical uncertainties are taken from the distribution of sequence values $\sigma_\gamma^2/N = (\langle A_\gamma^2\rangle - \langle A_\gamma\rangle^2)/N$, with N histogrammed eight-step sequence asymmetries. Table V lists the statistical uncertainties for each detector ring, for the uncorrected and background asymmetries, and the background corrected final asymmetry. For the background asymmetry and uncertainty we used the measured aluminum asymmetry [57] averaged over all four rings. The corrected asymmetry and uncertainty are calculated according to Eqs. (10) and (11). Any nonrandom effect such as those introduced by the correction factors $|\langle G(t_i)\rangle|$, $\Delta_{\rm dep}(t_i)$, $P_n(t_i)$, $\Delta_{sf}(t_i)$ are treated as systematic uncertainties. These enter as

$$\sigma_{\gamma,{\rm Sys}} = A_\gamma \sqrt{\left(\frac{\sigma_{P_n}}{P_n}\right)^2 + \left(\frac{\sigma_{\rm sf}}{\Delta_{\rm sf}}\right)^2 + \left(\frac{\sigma_G}{G}\right)^2 + \left(\frac{\sigma_{\rm dep}}{\Delta_{\rm dep}}\right)^2}$$

and are added in quadrature with the statistical uncertainty.

The uncertainties on the beam polarization and spin-flip efficiency were measured to be 5% and 1%, respectively. The uncertainty in the geometry factor is estimated to be below 1% from variations observed in the values when varying the step size in the Monte Carlo that was used to simulate the γ-ray interaction in the detectors. The uncertainty in the spin-flip scattering factor is estimated to be of the order of a few percent. Because the systematic uncertainties are scaled by the asymmetry, their contribution to the overall uncertainty in the asymmetry is negligible compared to the statistical uncertainty in the hydrogen asymmetry.

VII. CONCLUSION

The NPDGamma collaboration constructed a new cold neutron beam line (FP12 at LANSCE) dedicated for fundamental nuclear physics experiments. The first experiment at FP12 was NPDGamma. The NPDGamma collaboration has measured an upper limit for the parity-odd γ-ray asymmetry from polarized slow neutron capture on protons in a liquid parahydrogen target. We report a parity-odd asymmetry of $A_{\gamma,{\rm UD}} = [(-1.2 \pm 2.1\ ({\rm stat.}) \pm 0.2\ ({\rm sys.})] \times 10^{-7}$. We also report the first measurement of an upper limit for the PA left-right asymmetry in this reaction of $A_{\gamma,{\rm LR}} = [-1.8 \pm 1.9\ ({\rm stat.}) \pm 0.2\ ({\rm sys.})] \times 10^{-7}$. The measurement at FP12 was limited by neutron counting statistics. We carried out an extensive analysis of all systematic effects, backgrounds, and general performance diagnostics for the apparatus. The NPDGamma collaboration aims to make a measurement of the PV asymmetry in this reaction with an accuracy of 1×10^{-8}. We are currently installing the experiment at the Spallation Neutron Source (SNS) at Oak Ridge National Laboratory. With an improved neutron flux (projected to be a factor of 50 greater than at LANSCE FP12) and other increases in the figure of merit through several technical improvements, such as the use of a new supermirror polarizer and a reduction in γ backgrounds, we estimate that we can achieve this sensitivity in a reasonable time at SNS. We will resume the experiment at the SNS in 2011.

ACKNOWLEDGMENTS

The authors are deeply grateful to Mr. G. Peralta (LANL) for his dedication during the beam-line and experiment construction phases and for his extensive technical support during the experiment. The authors would like also to thank Mr. B. Teasdale (LANL) for his excellent design work in the experiment and for novel technical ideas, Mr. B. Etuk for his professional engineering support during the different phases of the beam-line and experiment constructions, Mr. W. Fox (CEEM) and Mr. T. Ries (TRIUMF) for the mechanical design of the detector array and the construction of the stand, and Mr. M. Kusner of Saint-Gobain in Newbury, Ohio, for interactions during the manufacture and characterization of the CsI(Tl) crystals. We would also like to thank TRIUMF for providing the personnel and infrastructure for the stand construction and the construction of the electronic gain modules. We thank Kevin Komicarsik, John Vanderwerp, and Jim Graham at CEEM and Jim Knudson at LANL for help with the liquid hydrogen target, various hydrogen target experts at national laboratories who participated in the hydrogen safety reviews, and the staff of the LANSCE facility for support during the construction and operation of the experiment. This work was supported in part by the US Department of Energy (Office of Energy Research, under Contract No. W-7405-ENG-36), the National Science Foundation (Grant Nos. PHY-0457219, PHY-0758018, and PHY-0100348), the NSF Major Research Instrumentation program (Grant No. NSF-0116146), for the procurement of the CsI crystals and neutron shielding, the Natural Sciences and Engineering Research Council of Canada (NSERC), and Japanese Grant-in-Aid for Scientific Research A12304014. The work of W.M.S. was supported in part by the Indiana University Center for Spacetime Symmetries. The development and application of ^{3}He spin filters used in this work were supported in part by the US Department of Energy, Office of Basic Energy Sciences, Division of Materials Sciences and Engineering, under Grant No. DE-FG02-03ER46093. The contributions from NIST were also supported through an Interagency Agreement with the US Department of Energy, Office of Nuclear Physics.

[1] M. J. Ramsey-Musolf and S. A. Page, Annu. Rev. Nucl. Part. Sci. **56**, 2 (2006).
[2] J. Erler and M. J. Ramsey-Musolf, Prog. Part. Nucl. Phys. **54**, 351 (2005).
[3] W. M. Snow, J. Res. Natl. Inst. Stand. Technol. **110**, 189 (2005).
[4] J. S. Nico and W. M. Snow, Annu. Rev. Nucl. Part. Sci. **55**, 27 (2005).
[5] C.-P. Liu, Phys. Rev. C **75**, 065501 (2007).
[6] J. F. Donoghue, E. Golowich, and B. Holstein, Phys. Rep. **31**, 319 (1986).
[7] D. H. Beck and B. Holstein, Int. J. Mod. Phys. E **10**, 1 (2001).
[8] D. H. Beck and R. D. McKeown, Annu. Rev. Nucl. Part. Sci. **51**, 189 (2001).
[9] D. H. Beck, Prog. Nucl. Part. Phys. **50**, 429 (2003).
[10] E. J. Beise, M. L. Pitt, and D. T. Spayde, Prog. Nucl. Part. Phys. **54**, 289 (2005).
[11] E. G. Adelberger and W. C. Haxton, Annu. Rev. Nucl. Part. Sci. **35**, 501 (1985).
[12] J. D. Bowman, G. T. Garvey, M. B. Johnson, and G. E. Mitchell, Annu. Rev. Nucl. Part. Sci. **43**, 829 (1993).
[13] S. Tomsovic, M. B. Johnson, A. Hayes, and J. D. Bowman, Phys. Rev. C **62**, 054607 (2000).
[14] C. S. Wood *et al.*, Science **275**, 1759 (1997).
[15] Y. B. Zeldovich, Sov. Phys. JETP **6**, 1184 (1957).
[16] V. V. Flambaum and I. B. Khriplovich, Sov. Phys. JETP **52**, 835 (1980).
[17] K. Tsigutkin, D. Dounas-Frazer, A. Family, J. E. Stalnaker, V. V. Yashchuk, and D. Budker, Phys. Rev. Lett. **103**, 071601 (2009).
[18] G. Prezeau, M. Ramsey-Musolf, and P. Vogel, Phys. Rev. D **68**, 034016 (2003).
[19] D. Kharzeev, R. D. Pisarski, and M. H. G. Tytgat, Phys. Rev. Lett. **81**, 512 (1998).
[20] G. S. Danilov, Phys. Lett. **18**, 40 (1965).
[21] J. Dai, M. J. Savage, J. Liu, and R. P. Springer, Phys. Lett. B **271**, 403 (1991).
[22] D. B. Kaplan and M. J. Savage, Nucl. Phys. A **556**, 653 (1993); **570**, 833 (1994); **580**, 679 (1994).
[23] E. M. Henley, W. -Y. P. Hwang, and L. S. Kisslinger, Phys. Lett. B **367**, 21 (1996).
[24] G. A. Lobov, Phys. At. Nucl. **65**, 534 (2002).
[25] W.-Y. P. Hwang and Chih-Yi Wen, arXiv:0803.0407 (2008).
[26] H. J. Lee, C. H. Hyun, C. H. Lee, and H. C. Kim, Eur. Phys. J. C **45**, 451 (2006).
[27] U. G. Meissner and H. Weigel, Phys. Lett. B **447**, 1 (1999).
[28] D. Gazit and H. Yee, Phys. Lett. B **670**, 154 (2008).
[29] B. Desplanques, J. F. Donoghue, and B. R. Holstein, Ann. Phys. **124**, 449 (1980).
[30] B. Desplanques, Phys. Rep. **297**, 1 (1998).
[31] S. L. Zhu *et al.*, Nucl. Phys. **748**, 435 (2005).
[32] D. R. Phillips, M. R. Schlinder, and R. P. Springer, Nucl. Phys. A **822**, 1 (2009).
[33] S. R. Beane and M. J. Savage, Nucl. Phys. B **636**, 291 (2002).
[34] *Scientific Grand Challenges: Forefront Questions in Nuclear Science and the Role of Computing at the Extreme Scale*, Workshop sponsored by the DOE Office of Nuclear Physics and the Office of Advanced Scientific Computing Research (2009).
[35] N. Christ, Proc. Sci., KAON2009, 027 (2009).
[36] J. F. Caviagnac *et al.*, Phys. Lett. B **67**, 148 (1977).
[37] S. C. Pieper and R. B. Wiringa, Annu. Rev. Nucl. Part. Sci. **51**, 53 (2001).
[38] R. Schiavilla, J. Carlson, and M. Paris, Phys. Rev. C **70**, 044007 (2004).
[39] B. Desplanques, Phys. Lett. B **512**, 305 (2001).
[40] C. H. Hyun, T.-S. Park, and D.-P. Min, Phys. Lett. B **516**, 321 (2001).
[41] C. H. Hyun, S. J. Lee, J. Haidenbauer, and S. W. Hong, Eur. Phys. J. A **24**, 129 (2005).
[42] C. A. Barnes *et al.*, Phys. Rev. Lett. **40**, 840 (1978); S. A. Page *et al.*, Phys. Rev. C **35**, 1119 (1987); H. C. Evans *et al.*, Phys. Rev. Lett. **55**, 791 (1985); M. Bini, T. F. Fazzini, G. Poggi, and N. Taccetti, *ibid.* **55**, 795 (1985).
[43] W. C. Haxton, Phys. Rev. Lett. **46**, 698 (1981).
[44] V. V. Flambaum and D. W. Murray, Phys. Rev. C **56**, 1641 (1997).
[45] G. S. Danilov, Phys. Lett. **18**, 40 (1965); Phys. Lett. B **35**, 579 (1971); Sov. J. Nucl. Phys. **14**, 443 (1972).
[46] M. R. Schindler and R. P. Springer, arXiv:0907.5358v1 (2010).
[47] C. H. Hyun, S. Ando, and B. Desplanques, Phys. Lett. B **651**, 257 (2007).
[48] P.-N. Seo *et al.*, Nucl. Instr. Meth. A **517**, 285 (2004).
[49] M. T. Gericke *et al.*, Nucl. Instr. Meth. A **540**, 328 (2005).
[50] W. S. Wilburn, J. D. Bowman, M. T. Gericke, and S. I. Penttilä, Nucl. Instr. Meth. A **540**, 180 (2005).
[51] T. E. Chupp *et al.*, Nucl. Instr. Meth. A **574**, 500 (2007).
[52] T. R. Gentile *et al.*, J. Res. Natl. Inst. Stand. Technol. **110**, 299 (2005).
[53] G. L. Jones *et al.*, Nucl. Instr. Meth. A **440**, 772 (2000).
[54] G. L. Jones *et al.*, Nucl. Instr. Meth. A **270**, 90 (1988).
[55] S. Santra *et al.*, Nucl. Instr. Meth. A **620**, 421 (2010).
[56] L. Barrón-Palos *et al.* (submitted to Nucl. Inst. Meth. A 2011).
[57] M. T. Gericke *et al.*, Phys. Rev. C **74**, 065503 (2006).
[58] W. B. Davenport and W. L. Root, *An Introduction to the Theory of Random Signals and Noise* (John Wiley & Sons, New York, 1987).
[59] M. T. Gericke *et al.*, J. Res. Natl. Inst. Stand. Technol. **110**, 215 (2005).
[60] J. D. Bowman and J. C. Vanderleeden, Nucl. Instr. Meth. **85**, 19 (1970).
[61] P.-N. Seo *et al.*, Phys. Rev. ST Accel. Beams. **11**, 084701 (2008).

[62] C. Amsler *et al.*, Phys. Lett. B **667**, 1 (2008).

[63] A. R. Edmonds, *Angular Momentum in Quantum Mechanics* (Princeton University Press, Princeton, NJ, 1957).

[64] F. Bloch, Phys. Rev. **50**, 272 (1936).

[65] C. S. Wang Chang and D. L. Falkolf, Phys. Rev. **76**, 365 (1949).

[66] Y.-S. Tsai, Rev. Mod. Phys. **46**, 815 (1974).

[67] M. J. Berger *et al.*, Stopping-power and range tables for electrons, protons, and helium ions [http://physics.nist.gov/PhysRefData/Star/Text/PSTAR.html].

[68] J. D. Jackson, *Classical Electrodynamics*, 2nd ed. (Wiley, New York, 1975), p. 705.

[69] M. T. Gericke, J. D. Bowman, and M. B. Johnson, Phys. Rev. C **78**, 044003 (2008).

[70] A. Csótó, B. F. Gibson, and G. L. Payne, Phys. Rev. C **56**, 631 (1997).

[71] J. D. Bowman (private communication 2010).

[72] A. N. Bazhenov *et al.*, Phys. Lett. B **289**, 17 (1992).

[73] V. A. Vesna *et al.*, Phys. Rev. C **77**, 035501 (2008).

[74] V. A. Vesna *et al.*, JETP Lett. **36**, 209 (1982).

[75] M. Avenier *et al.*, Nucl. Phys. A **436**, 83 (1985).

[76] G. S. Mitchell *et al.*, Nucl. Instr. Meth. A **521**, 468 (2004).